

Formation of first star clusters under the supersonic gas flow – II. Critical halo mass and core mass function

Shingo Hirano^{1,2}★

¹*Department of Applied Physics, Faculty of Engineering, Kanagawa University, Kanagawa 221-0802, Japan*

²*Department of Astronomy, School of Science, University of Tokyo, Tokyo 113-0033, Japan*

30 January 2025

ABSTRACT

The formation and mass distribution of the first stars depend on various environmental factors in the early universe. We compare 120 cosmological hydrodynamical simulations to explore how the baryonic streaming velocity (SV) relative to dark matter affects the formation of the first stars. We vary SV from zero to three times its cosmic root-mean-square value, $v_{\text{SV}}/\sigma_{\text{SV}} = 0 - 3$, and identify 20 representative halos from cosmological simulations. For each model, we follow the evolution of a primordial star-forming cloud from the first appearance of a dense core (with gas density $> 10^6 \text{ cm}^{-3}$) until 2 Myr later. In each model, higher SV systematically delays the formation of primordial clouds, formed inside more massive halos ($10^5 - 10^7 M_{\odot}$), and promotes cloud-scale fragmentation and multiple-core formation. The number and total mass of dense cores increase with increasing SV. More than half of models with $v_{\text{SV}}/\sigma_{\text{SV}} \geq 1.5$ form three or more dense cores in a single halo. In extreme cases, up to 25 cores form at once, which leaves a massive first star cluster. On the other hand, models with $v_{\text{SV}}/\sigma_{\text{SV}} \leq 1$ form only one or two cores in a halo. In addition, HD-cooling is often enabled in models with low SV, especially in low- z , where HD-cooling is enabled in more than 50% of models. This leads to the formation of the low-mass first star. SV shapes the resulting initial mass function of the first stars and plays a critical role in setting the star-forming environment of the first galaxies.

Key words: methods: numerical – dark ages, reionization, first stars – stars: Population III – stars: formation – stars: black holes

1 INTRODUCTION

The formation of the first stars, or Population III (Pop III) stars, marks a key transition in cosmic history. It shapes the earliest stages of galaxy evolution and the chemical enrichment of the universe (see [Klessen & Glover 2023](#), for a review). Recent advances in observational facilities, notably the James Webb Space Telescope (JWST) and the Atacama Large Millimeter/submillimeter Array (ALMA), have begun to probe the cosmic dawn, enabling the study of galaxies at redshifts as high as $z = 10 - 15$ (e.g., [Robertson et al. 2024](#); [Harikane et al. 2024](#)). As we enter this “deep universe era,” ongoing and planned facilities – such as the Thirty Meter Telescope (TMT) and the Giant Magellan Telescope (GMT) – promise even deeper insights into the birth of the first galaxies and their stellar populations.

Despite these observational leaps, the direct detection of the first stars remains elusive. Instead, their initial mass function (IMF) constraints rely on indirect evidence. Extremely metal-poor (EMP) stars in the Milky Way and dwarf galaxies carry the chemical imprint of the first supernovae, allowing researchers to infer the IMF of the earliest stellar generations (e.g., [Keller et al. 2014](#); [Bessell et al. 2015](#); [Rossi et al. 2024](#), and also see [Figure 1](#)). However, these data remain incomplete, and certain mass ranges, such as those leading to direct black hole formation, are not directly constrained. Thus, theoretical models and numerical simulations are central to understanding how the first stars formed and how their mass distribution emerged.

One of the external factors influencing the primordial star formation process is the streaming velocity (SV): the relative, supersonic motion between baryonic gas and dark matter (DM) imprinted at cosmic recombination ([Tseliakhovich & Hirata 2010](#); [Fialkov 2014](#)). This effect is not merely a subtle perturbation; it can qualitatively alter the conditions of star formation. Enhanced SV values delay the onset of gas collapse, shift star formation to more massive DM halos, increase the characteristic gas mass scale, and thereby shape the IMF of the first stars (e.g., [Greif et al. 2011](#); [Stacy et al. 2011](#); [Naoz & Narayan 2014](#)). [Figure 2](#) visualizes the impact of SV on the first star formation based on a set of cosmological simulations ([Hirano et al. 2017, 2018](#)). Moreover, SV can give rise to unique phenomena, such as Supersonically Induced Gas Objects (SIGOs), which form in regions where SV suppresses DM clustering and gas assembles into dense, star-forming structures with low DM content (e.g., [Chiou et al. 2018, 2019](#)). SIGOs may represent a new pathway for globular cluster formation, bridging conditions in the high-redshift universe to the present-day population of globular clusters.

While numerous simulations have explored the baseline scenario of the first star formation under standard conditions without significant SV, recent studies have begun to systematically incorporate SV and other environmental parameters, such as external radiation ([Schauer et al. 2021](#); [Kulkarni et al. 2021](#)). Among these works, we focus on how SV influences the formation of primordial star-forming gas clouds within DM halos. Our prior work ([Hirano et al. 2023](#), hereafter [Paper I](#)) introduced a methodology for characterizing the formation of the first star clusters under different SV.

★ E-mail: shingo-hirano@kanagawa-u.ac.jp

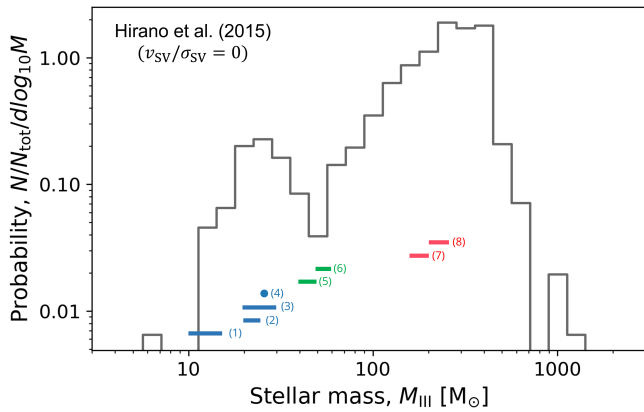


Figure 1. Comparison of the theoretical estimation of the stellar mass distribution of the first stars (Hirano et al. 2015) with indirect observational clues regarding the mass range of the parent first star; (A) Core-collapse supernovae (CCSN; $10 - 40 M_{\odot}$): (1) LMC-119 (Chiti et al. 2024), (2) HE 0020-1741 (Placco et al. 2016), (3) SDSS J102915+172927 (Caffau et al. 2011; Schneider et al. 2012), LAMOST J221750.59+210437.2 (Aoki et al. 2018), 2MASS J20500194-6613298 (Mardini et al. 2024), (4) SMSS J031300-670839.3 (Keller et al. 2014; Bessell et al. 2015), (B) Hypernova ($40 - 60 M_{\odot}$): (5) SPLUS J210428.01-004934.2 (Placco et al. 2021), (6) AS0039 (Skúladóttir et al. 2021), (C) Pair-instability supernovae (PISN; $140 - 260 M_{\odot}$): (7) LAMOST J1010+2358 (Xing et al. 2023), (8) SDSS J001820.5-093939.2 (Aoki et al. 2014).

In this second paper, we systematically investigate the SV effect on the first star formation. Extending our previous study (Hirano et al. 2023), we perform a parameter survey by selecting 20 representative DM halos and applying six different SV amplitudes (0, 1, 1.5, 2, 2.5, and 3 times the cosmic root-mean-square value). By following the evolution of primordial gas clouds until 2 Myr after the cloud collapse, we analyze the formation of multiple dense cores where $n \geq 10^6 \text{ cm}^{-3}$ within a single halo, derive the core mass function, and identify the critical halo mass scales that govern when and where first star clusters appear. This results in 120 distinct zoom-in simulations that allow us to explore how SV influences the onset of star formation and the mass distribution of primordial gas clouds.

This paper is organized as follows. Section 2 describes simulation methods and initial conditions. Section 3 presents the results of our parameter survey, focusing on the critical halo mass and the resulting core mass functions. Section 4 discusses the implications of our findings for the IMF of Pop III stars and the formation of first star clusters. Finally, Section 5 summarizes our conclusions and outlines directions for future work in this series.

2 NUMERICAL METHODOLOGY

We perform a set of three-dimensional cosmological hydrodynamical simulations to study the dependence of first star formation under the baryonic streaming motions in the early universe. The simulation setup follows Paper I. However, we reduce the numerical resolution to simulate the long-term evolution of the primordial star-forming gas clouds. Furthermore, we increase the number of host haloes for which we study the effects of the baryonic streaming motion from seven to twenty samples to be able to discuss the dependence on the formation environment in more detail.

2.1 Initial condition

We first select 20 DM halos with masses of $10^5 - 10^6 M_{\odot}$ from large-scale cosmological simulations that assume no initial streaming velocity. We then apply a hierarchical zoom-in technique to refine each halo step by step, ultimately achieving a mass resolution of about $0.03 M_{\odot}$ for gas particles. Finally, we introduce a uniform relative velocity between DM and baryons ($v_{\text{SV}}/\sigma_{\text{SV}} = 0 - 3$) for each zoom-in initial condition, resulting in a total of 120 distinct models.

We first use the public code MUSIC (Hahn & Abel 2011) to generate the base cosmological ICs for a comoving volume of $L_{\text{box}} = 10 h^{-1}$ comoving megaparsec (cMpc) per side at $z_{\text{ini}} = 499$. Our adopted Λ CDM cosmology (Planck Collaboration et al. 2020) has $\Omega_{\text{m}} = 0.31$, $\Omega_{\text{b}} = 0.048$, $\Omega_{\Lambda} = 0.69$, $H_0 = 68 \text{ km s}^{-1} \text{ Mpc}^{-1}$, $\sigma_8 = 0.83$, and $n_s = 0.96$.

We then run cosmological N -body/hydrodynamics simulations using GADGET-3 (Springel 2005). We identify the first DM halo that forms in each cosmological IC without streaming motion and re-simulate it at higher resolution using hierarchical zoom-in ICs generated by MUSIC. With five levels of refinement, the effective resolution improves from 512^3 to 16384^3 , reducing the DM particle mass from $9.426 \times 10^5 M_{\odot}$ to $28.76 M_{\odot}$. We obtain 20 such zoomed-in halos. Seven of these correspond to Halos A-G in Paper I (see the caption of Table A1).

We introduce a uniform initial relative velocity between the DM and baryonic components along the x -axis to model the baryonic streaming motion. Because the coherence length of the streaming velocity field extends over a few megaparsecs, well beyond the scale of our DM halos, assuming a uniform velocity is appropriate. Under the baryons-trace-dark-matter (BTD) approximation (Park et al. 2020, 2021), we assume that the initial baryon density matches the DM density distribution. We generate six sets of ICs, each sharing the same density phase but differing in their initial streaming velocity: $v_{\text{SV}}/\sigma_{\text{SV}} = 0, 1, 1.5, 2, 2.5,$ and 3 , normalized by the root-mean-square velocity $\sigma_{\text{SV}}(z) = \sigma_{\text{SV}}^{\text{rec}}(1+z)/(1+z_{\text{rec}}) = 13.76 \text{ km s}^{-1}$ at $z_{\text{ini}} = 499$. This value is derived from $\sigma_{\text{SV}}^{\text{rec}} = 30 \text{ km s}^{-1}$ at the cosmic recombination era ($z_{\text{rec}} = 1089$).

In total, we have 120 models: twenty DM halo combined with six different streaming velocities. Table A1 lists these models, where the model names are defined by a halo ID (I01-I20) and a velocity label (V00, V10, V15, V20, V25, and V30).

2.2 Cosmological simulation

We perform the cosmological simulations with a modified version of the parallel N -body/smoothed particle hydrodynamics (SPH) code GADGET-3 (Springel 2005), adapted for metal-free star formation (Hirano et al. 2018), and including detailed non-equilibrium chemistry of 14 species (e^- , H, H^+ , H^- , He, He^+ , He^{++} , H_2 , H_2^+ , D, D^+ , HD, HD^+ , HD^-) as in Yoshida et al. (2007, 2008). To follow gas collapse down to $n_{\text{th}} = 10^6 \text{ cm}^{-3}$, we apply a hierarchical refinement scheme that ensures the local Jeans length is always resolved. Specifically, we require that 15 times the smoothing length is less than the local Jeans length (or about 1000 SPH particle mass is less than the local Jeans mass), and we increase resolution through the particle splitting technique (Kitsionas & Whitworth 2002). This yields minimum particle masses of $m_{\text{DM},\text{min}} = 0.1439 M_{\odot}$ for DM and $m_{\text{gas},\text{min}} = 0.02636 M_{\odot}$ for gas.

We follow the evolution for 2 Myr after the gas cloud first reaches $n_{\text{th}} = 10^6 \text{ cm}^{-3}$. We define $t_{\text{th}} = 0 \text{ yr}$ as the time when the collapsing gas cloud in each model reaches this threshold density. To

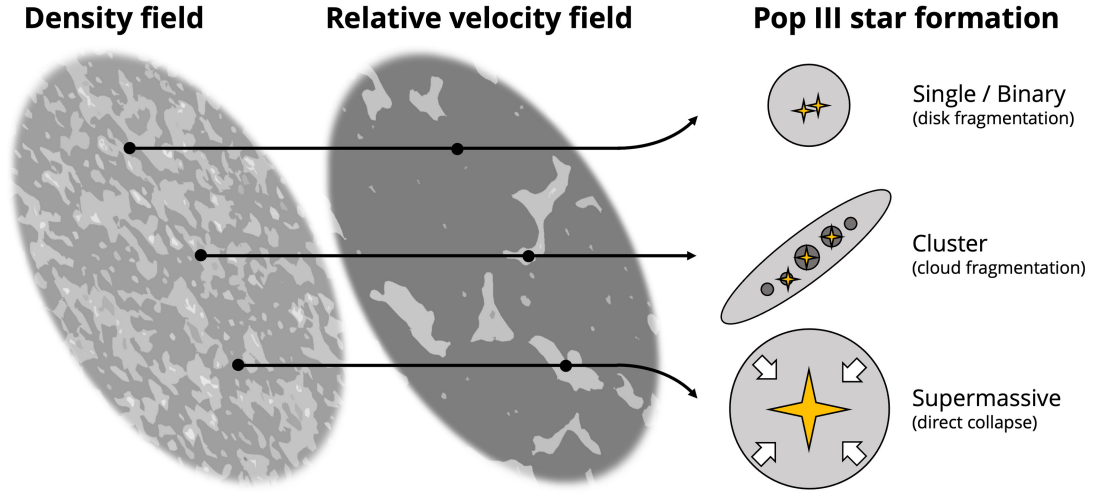


Figure 2. Schematic diagram of the dependence of the first star formation process on baryonic supersonic motions relative to dark matter in the early universe. While the typical first star formation process proceeds in regions with negligible relative velocities, multiple star-forming gas clouds can form due to cloud-scale fragmentation in areas with low relative velocities, and supermassive first stars can form from the direct collapse process in regions with high relative velocities.

enable such long-term evolution, we adopt an opaque core approach (Hirano & Bromm 2017), artificially suppressing the gas cooling rate above n_{th} :

$$\Lambda_{\text{red}} = \beta_{\text{esc,art}} \cdot \Lambda_{\text{thin}}, \quad (1)$$

with an artificial escape fraction and an artificial optical depth as

$$\beta_{\text{esc,art}} = \frac{1 - \exp(-\tau_{\text{art}})}{\tau_{\text{art}}}, \quad \tau_{\text{art}} = \left(\frac{n}{n_{\text{th}}}\right)^2. \quad (2)$$

This enhancement in effective optical depth halts further collapse, allowing us to study the large-scale evolution of the star-forming region. We also omit unnecessary chemistry calculations for gas particles above n_{th} . Note that 2 Myr is shorter than the typical lifetime of a first star (Schaerer 2002), so no supernova feedback affects our halos during this period.

3 FIRST STAR FORMATION UNDER THE SUPERSONIC GAS FLOW

Figure 3 is the distribution of redshift and virial halo mass (z - M_V diagram) when the maximum density of the collapsing gas cloud first reaches $n_{\text{th}} = 10^6 \text{ cm}^{-3}$ (defined as $t_{\text{th}} = 0 \text{ yr}$). The sub-panels show probability density distributions of z (top) and M_V (right) for each streaming velocity (v_{SV}). At higher v_{SV} , the gravitational collapse of the primordial star-forming cloud delays (resulting in a decrease in z as shown in the top panel), and the host DM halo grows in mass (leading to an increase in M_V as shown in the right panel). As a result, in the z - M_V diagram, the models move from the bottom-right to the top-left with increasing v_{SV} , as confirmed by previous studies. In addition to the SV dependence, another variation from the bottom-left to the top-right is orthogonal to the first correlation. The second dependence is due to differences in the magnitude of the primordial density fluctuations that gave rise to the halo (I01-I20).

Table A1 summarises the results for 120 models. To investigate the statistical properties of the SV dependence on the first star formation, we average the analysis results for each SV value across the five classes as Table 1:

- *All* shows the averaged values of all models for each SV value.

- *High*, *Middle*, and *Low* show averaged values of three groups, the top-right, middle, and bottom-left populations on z - M_V diagram (Figure 3) to study the dependence of the magnitude of primordial density fluctuation.

- *HD* shows the averaged values of models in which the hydrogen deuteride (HD)-cooling is effective.

Figure 4 shows the z - M_V diagram for *All*, *High*, *Middle*, and *Low* classes.

In the following subsections, we show the SV dependence of the physical quantities at three scales: the virial DM halo, which is the gravitationally bound system (Section 3.1), the Jeans gas cloud, which is unstable to the gravitational collapse (Section 3.2), and the dense core, arbitrarily defined by the maximum numerical resolution of this study, n_{th} , where the first star(s) form (Section 3.3).

3.1 Virial dark matter halo

We begin by examining how the baryonic SV affects the formation epoch and mass scale of the first star-forming DM halos, which are essential for constructing semi-analytic models and linking initial conditions to subsequent star formation events. Figure 3 is the distribution of the redshift (z) and virial halo mass (M_V) at the onset of gas cooling and collapse for all models in this study. For models without SV effect ($v_{\text{SV}}/\sigma_{\text{SV}} = 0$; V00), our sample of 20 models spans broad ranges in formation times ($z = 16.52 - 36.80$) and halo masses ($M_V = 2.195 \times 10^5 - 8.400 \times 10^6 M_\odot$). These halos have the virial temperatures $T_V \sim 1000 - 3000 \text{ K}$, consistent with standard H_2 -cooling minihalos,

$$M_V = 8.120 \times 10^5 M_\odot h^{-1} \left(\frac{T_V}{2000 \text{ K}}\right)^{3/2} \left(\frac{1+z}{25}\right)^{-3/2}. \quad (3)$$

On average, the formation epoch is $\bar{z} = 27.07$ and the virial mass $\bar{M}_V = 1.072 \times 10^6 M_\odot$ for the no-SV models (Class A00 in Table 1).

Introducing SV affects the conditions under which gas cooling and collapse begin in a DM minihalo (i.e., z and M_V). For the same cosmological density fluctuation, a stronger SV influence leads to a delay in the formation epoch and an increase in the virial halo mass, which results in the move from the bottom-right toward the top-left

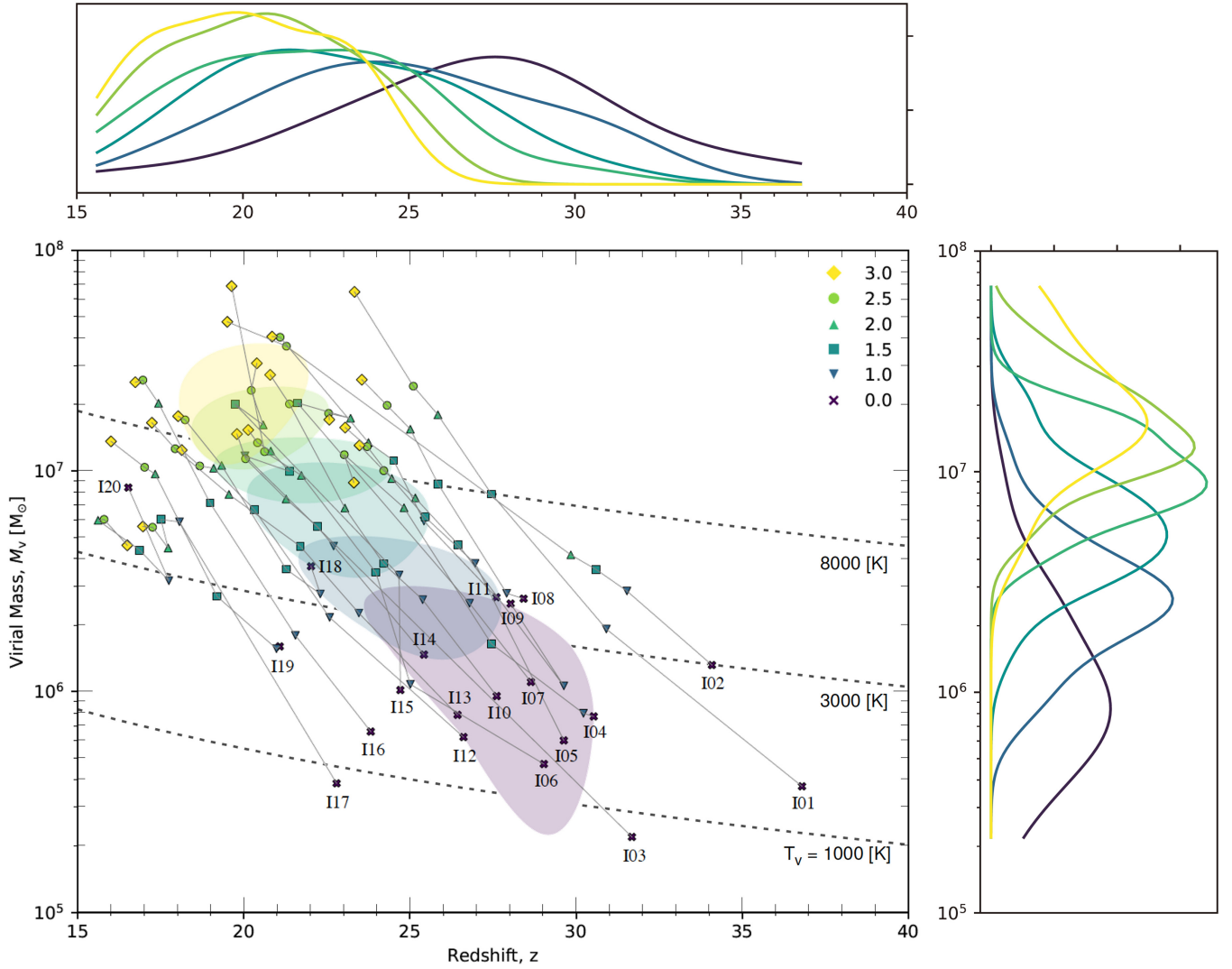


Figure 3. Distribution of redshift and virial halo mass (z - M_v diagram) for 120 models. The colours and symbols correspond to the magnitude of the initial streaming velocity (V00-V30 with $v_{SV}/\sigma_{SV} = 0, 1, 1.5, 2, 2.5, \text{ and } 3$). The solid lines connect models that examined identical density fluctuations (I01-I20). We compute the mean and variance of the data for each streaming velocity and generate histograms using the Kernel Density Estimation (top and right panels). The coloured areas in the central panel show z - M_v distributions for each initial streaming velocity. The dashed lines show the virial masses for three different virial temperatures, $T_v = 1000, 3000, \text{ and } 8000$ K (Equation 3).

in the z - M_v diagram (Figure 3). As an example, consider I01, the density fluctuation that undergoes the earliest halo growth among those examined in this study. Since the SV amplitude decreases with time as $v_{SV} \propto (1+z)$, the earliest-forming DM halo (I01) experiences the strongest SV effect of all models (I01-I20). For I01, going from $v_{SV}/\sigma_{SV} = 0$ to 3 decreases z by $z' - z = dz = 13.47$ and increases M_v by a factor of $M'_v/M_v = \Delta M_v = 173$, the largest difference in our sample. While the gas cloud within the DM minihalo struggles to collapse, the large-scale structure around the halo continues to grow, forming more substantial filament and knot (Figure 5). As a result, by the time the primordial gas cloud finally begins to contract, the distribution of surrounding matter differs significantly from that in the no-SV case (I01V00). We also confirm that during the delayed formation epoch, the ongoing formation and mergers of minihalos contribute to halo growth.

Next, we examine the response of the DM halo formation from 20 primordial density fluctuations to six different SV values on z -

M_v diagram (Figure 3). Starting with the smallest SV amplitude in our parameter set (V10 with $v_{SV}/\sigma_{SV} = 1$), we immediately see a large shift in the z - M_v diagram compared to the no-SV model (V00). Averaging over all models with this same SV amplitude (V10 in Table 1) and comparing them to the no-SV case (V00), we find that increasing SV from $v_{SV}/\sigma_{SV} = 0$ to 1 changes the formation redshift by $dz = 2.38$ and increases M_v by a factor of $\Delta M_v \sim 2.46$. Because $v_{SV}/\sigma_{SV} = 1$ is close to the most probable SV value in the universe, $v_{SV}/\sigma_{SV} \sim 0.8$ (Tselikhovich & Hirata 2010), this result highlights the importance of accounting for SV in modelling the overall first star formation process. As we increase SV further, both dz and ΔM_v generally grow larger, reflecting stronger SV, induced delays and mass enhancements in halo formation. A subset of models even surpasses $T_v = 8000$ K, where atomic hydrogen cooling becomes relevant, though ultimately all halos in our sample rely on H_2 -cooling during collapse (see Section 3.2). Interestingly, for $v_{SV}/\sigma_{SV} = 2.5 - 3$, we discover an inverse trend: lower-redshift collapses occur at lower

Table 1. Simulation results averaged for each classified model

Class	$v_{\text{SV}}/\sigma_{\text{SV}}$	\bar{z}	$\overline{R_v}$ (pc)	$\overline{M_v}$ (M_\odot)	$\overline{f_b}$	N_{HD}/N	$\overline{N_c}$	$\overline{M_{c,\text{tot}}}$ (M_\odot)	$\overline{\epsilon_{\text{III}}}$	$\overline{M_{c,1}}$ (M_\odot)	$\overline{M_{c,2}}$ (M_\odot)	$\overline{q_c}$
<i>(All)</i>												
A00	0.0	27.07	122.3	1.072×10^6	0.133	0.20	1.55	6445	0.0453	5856	975	0.166
A10	1.0	24.69	178.9	2.637×10^6	0.129	0.35	1.60	8729	0.0257	7525	4072	0.541
A15	1.5	22.83	251.2	5.838×10^6	0.126	0.25	3.25	13794	0.0188	10638	2597	0.244
A20	2.0	21.78	314.4	9.695×10^6	0.123	0.10	5.20	19940	0.0167	14331	4221	0.295
A25	2.5	20.49	380.2	1.503×10^7	0.122	0	4.60	22876	0.0125	16284	4701	0.289
A30	3.0	20.00	421.7	1.908×10^7	0.121	0.05	4.65	20514	0.0089	14284	3567	0.250
<i>(High)</i>												
H00	0.0	30.99	120.2	1.540×10^6	0.124	0	1	11407	0.0598	11407	-	-
H10	1.0	29.08	147.9	2.491×10^6	0.121	0.20	1.20	11043	0.0367	10149	4089	0.403
H15	1.5	26.97	218.8	6.610×10^6	0.114	0.20	4.60	19929	0.0266	14374	1861	0.129
H20	2.0	25.92	269.2	1.031×10^7	0.113	0	7.60	30962	0.0267	18326	5262	0.287
H25	2.5	23.20	389.0	2.345×10^7	0.119	0	5.60	33337	0.0120	17958	6815	0.380
H30	3.0	22.14	457.1	3.345×10^7	0.125	0	7.60	33322	0.0080	20148	7594	0.377
<i>(Middle)</i>												
M00	0.0	28.41	101.4	7.240×10^5	0.128	0.25	1.88	4198	0.0453	3670	668	0.182
M10	1.0	25.22	177.8	2.808×10^6	0.123	0.25	2.00	10694	0.0308	8468	6448	0.761
M15	1.5	23.25	254.8	6.458×10^6	0.122	0.38	4.25	15663	0.0199	10604	2937	0.277
M20	2.0	22.49	307.3	1.005×10^7	0.120	0.13	4.88	20360	0.0170	16171	4291	0.265
M25	2.5	21.49	360.0	1.488×10^7	0.119	0	6.00	24086	0.0136	16265	7174	0.441
M30	3.0	21.21	409.7	2.045×10^7	0.114	0.13	5.00	30311	0.0130	21134	4765	0.225
<i>(Low)</i>												
L00	0.0	22.75	153.4	1.296×10^6	0.144	0.29	1.57	6998	0.0374	6204	2508	0.404
L10	1.0	20.95	206.2	2.557×10^6	0.140	0.57	1.43	5852	0.0163	5310	1621	0.305
L15	1.5	19.40	272.7	4.761×10^6	0.139	0.14	1.14	9172	0.0139	8613	6579	0.764
L20	2.0	18.01	360.7	8.905×10^6	0.136	0.14	3.86	14220	0.0118	10472	3332	0.318
L25	2.5	17.41	398.1	1.106×10^7	0.127	0	2.29	16480	0.0118	15205	2265	0.149
L30	3.0	17.08	411.4	1.181×10^7	0.125	0	2.14	9285	0.0063	7140	1085	0.152
<i>(HD)</i>												
D00	0.0	25.99	122.3	1.013×10^6	0.140	-	2.75	4406	0.0310	3555	581	0.164
D10	1.0	23.78	172.1	2.181×10^6	0.128	-	1	3947	0.0142	3947	-	-
D15	1.5	24.30	213.8	4.373×10^6	0.125	-	2.80	6384	0.0117	5382	597	0.111
D20	2.0	21.19	298.5	8.470×10^6	0.136	-	6.50	11563	0.0101	8884	706	0.080
D25	2.5	-	-	-	-	-	-	-	-	-	-	-
D30	3.0	22.57	354.8	1.705×10^7	0.109	-	1	7494	0.0040	7494	-	-

Notes. Column 1: classification name. Column 2: relative streaming velocity normalized by the root-mean-square value ($v_{\text{SV}}/\sigma_{\text{SV}}$). Column 3: redshift (z) when the gas number density firstly reaches $n_{\text{H}} = 10^6 \text{ cm}^{-3}$. Columns 4-6: radius (R_v), mass (M_v), and baryon fraction (f_b) at the virial scale. Column 7: proportion of the HD-cooling models that meet the abundance ratio criterion $f_{\text{HD}}/f_{\text{H}_2} \geq 10^{-3}$ at the end of the calculation $t_{\text{th}} = 2 \text{ Myr}$. Column 8: number of cores (N_c). Column 9: the total mass of cores ($M_{c,\text{tot}}$). Column 10: mass conversion efficiency ($\epsilon_{\text{III}} = M_{c,\text{tot}}/(f_b M_v)$). Columns 11 and 12: mass of the primary and secondary core ($M_{c,1}$ and $M_{c,2}$). Column 13: mass ratio of the primary and secondary cores ($q_c = M_{c,2}/M_{c,1}$). Table A1 shows all data for each model. We average the results of all models (*All*), three classified groups (*High*, *Middle*, and *Low*), and models with HD-cooling enabled (*HD*) for 6 different initial streaming velocities: (*High*) I01, I02, I08, I09, I11, (*Middle*) I03-07, I10, I14, I15, (*Low*) I12, I13, I16-20, and (*HD*) see column 7 in Table A1. There is no data in columns 12 and 13 for H00, D10, and D30 because none of the models belonging to them have a secondary core.

halo masses, contrary to the behaviour in models with lower $v_{\text{SV}}/\sigma_{\text{SV}}$ (coloured areas in Figure 3). This finding suggests a new dependence on SV, indicating that the slope of the critical halo mass versus redshift relation may change sign at high SV amplitudes.

The effects of SV on halo properties also vary with the formation epoch. Halos that form at higher redshifts experience larger changes in both redshift and virial mass (z and M_v) when SV is increased, compared to halos forming at lower redshifts (Figure 3). As the amplitude of SV decreases over time according to $v_{\text{SV}} \propto (1+z)$, even in regions with initially high SV, the influence of SV becomes weaker if the magnitude of density fluctuations is small and structure formation delays. To perform a quantitative comparison, we classify halos into three groups based on their formation epoch (*High*, *Middle*, and *Low*) and average their physical properties (Table 1). Figure 4

reveals that the distance of averaged properties on z - M_v diagram for *High* group is longer than one for *Low* group. On the other hand, at $v_{\text{SV}}/\sigma_{\text{SV}} = 1-2$, the virial mass remains approximately constant among 3 groups, whereas at $v_{\text{SV}}/\sigma_{\text{SV}} = 2.5-3$, *Low* group collapses at lower M_v compared to *High* group. When modelling the effect of SV on the critical halo mass, the formation epoch must be accounted for by adjusting the influence of SV accordingly.

Figure 6 summarizes the average physical quantities for all models and each group as a function of SV magnitude. *All* in the main panels represents the average values of physical quantities for each SV, demonstrating that the average values depend on the SV magnitude. The sub-panels show the distribution of each physical quantity for each SV, confirming that SV determines not only the mean values but also the distribution shapes and variances. Re-

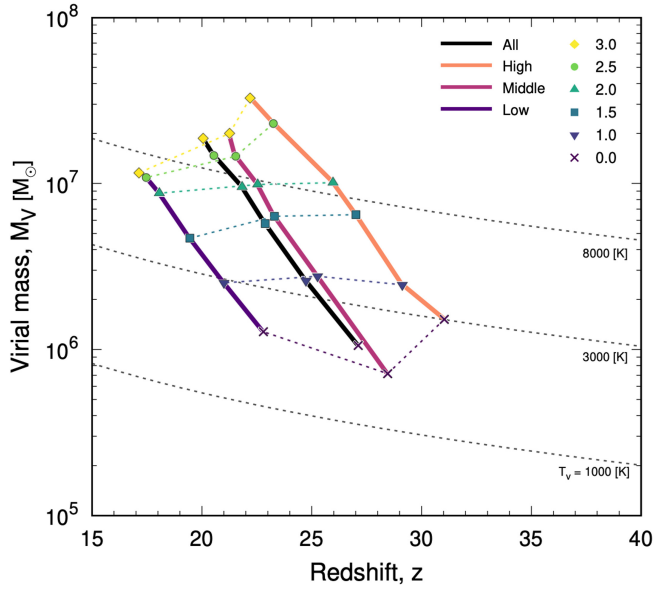


Figure 4. z - M_V diagram as Figure 3 but for averaged results: *All* for all models and *High*, *Middle*, and *Low* for the top-right, middle, and bottom-left populations on Figure 3 (see also the caption of Table 1).

turning to the main panels, the grey lines in the background illustrate the SV dependence of physical quantities for each model (I10-I20), and their averaged values are classified into three groups, *High*, *Middle*, *Low*. Figure 6(a) and (b) show the dependence of z and M_V discussed above. Figure 6(c) shows the baryon fraction, $f_b = M_b / (M_b + M_{DM}) = M_b / M_V$. f_b within the DM halos is generally below the cosmic mean, $\Omega_b / \Omega_m = 0.15484$ (horizontal dotted line), and decreases with increasing v_{SV} / σ_{SV} . This aligns with the known tendency of SV to inhibit baryon accretion into halos. An exception is the *High* group at $v_{SV} / \sigma_{SV} = 2 - 3$, where f_b increases due to the large SV at high redshift, causing the selective inflow of gas into DM halos to be trapped by the strong gravitational potential of massive DM halos.

3.1.1 Exceptional correlation

As confirmed thus far, generally, as the magnitude of SV in the halo formation region increases from $v_{SV} / \sigma_{SV} = 0$ to 3, halo formation delays and halo mass increases (lower redshift z and higher halo mass M_V). However, a small subset of models ($\sim 10\%$) shows a different trend, for example, where collapse occurs at higher z and lower M_V . We classify the relevant models into three exceptional categories (*E1*, *E2*, and *E3*) according to the increase or decrease in z and M_V compared to models with smaller SV (Column 7 in Table A1).

- *E1* as earlier formation of lighter halos (increase of z and decrease of M_V): 10 models, I03V15, I04V30, I07V20, I07V30, I09V10, I15V20, I17V20, I18V10, I20V10, I20V30.
- *E2* as earlier formation of heavier halos (increases of both z and M_V): 2 models, I15V30, I20V25.
- *E3* as later formation of lighter halos (decreases of both z and M_V): 2 models, I16V30, I19V10.

While most models (106 models) follow the general trend of delayed formation and increased halo mass with higher SV, a subset of models (14 models) deviates from this relation. These deviations suggest that SV's influence on halo formation is not uniform across all den-

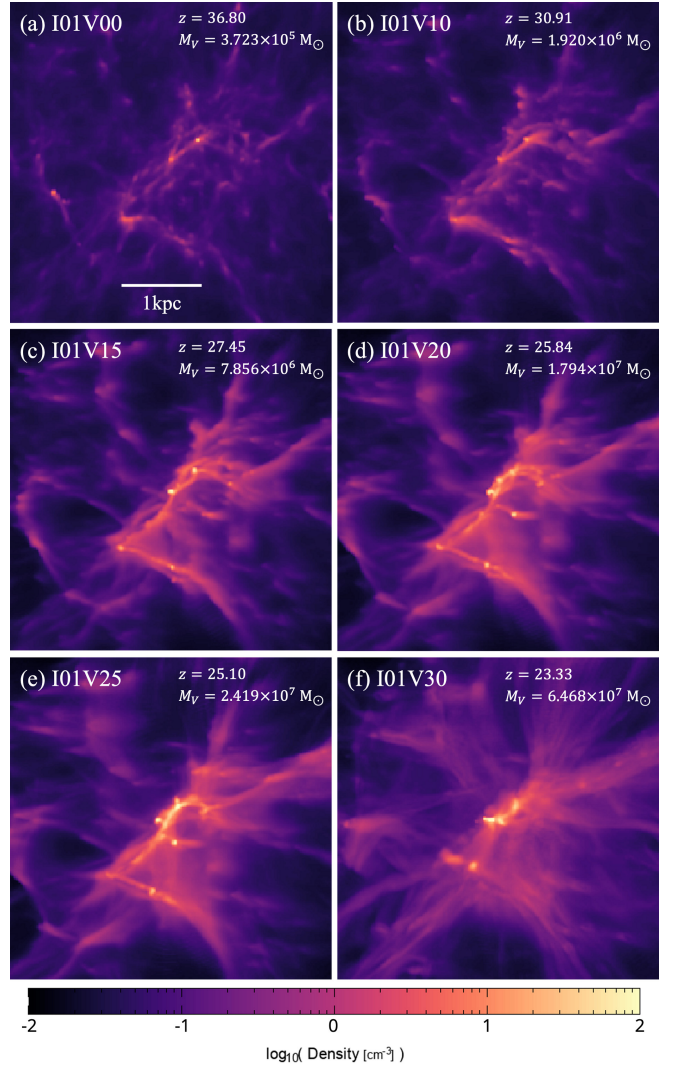


Figure 5. Projected density distribution around the density centre at the completion of gas cloud contraction (when $t_{th} = 0$ yr) of I01 models. The direction of the initial relative velocity between DM and gas components is aligned with the horizontal axis (from left to right) in the figure.

sity fluctuations and may depend on additional factors such as local density environments or merger histories.

3.2 Jeans gas cloud

By examining the properties of DM halos, we can investigate the conditions under which the first stars form, specifically, when and where they form. Conversely, by analyzing gas cloud properties, we can explore the mass distribution of the first stars. As discussed in Section 3.1, the magnitude of SV alters the physical properties (z , M_V , and f_b) of the DM halos where primordial stars form. Consequently, the physical properties of the star-forming gas clouds within these halos are also influenced by SV. In particular, the physical quantities at the Jeans scale of the star-forming gas clouds critically determine the star formation process of primordial stars. To investigate how the magnitude of SV affects gas clouds' physical properties, we plotted the radial profiles of density, temperature, and accretion rate as functions of radius from the dense core (Figure 7). To determine whether the SV dependence of gas cloud properties varies with the halo's

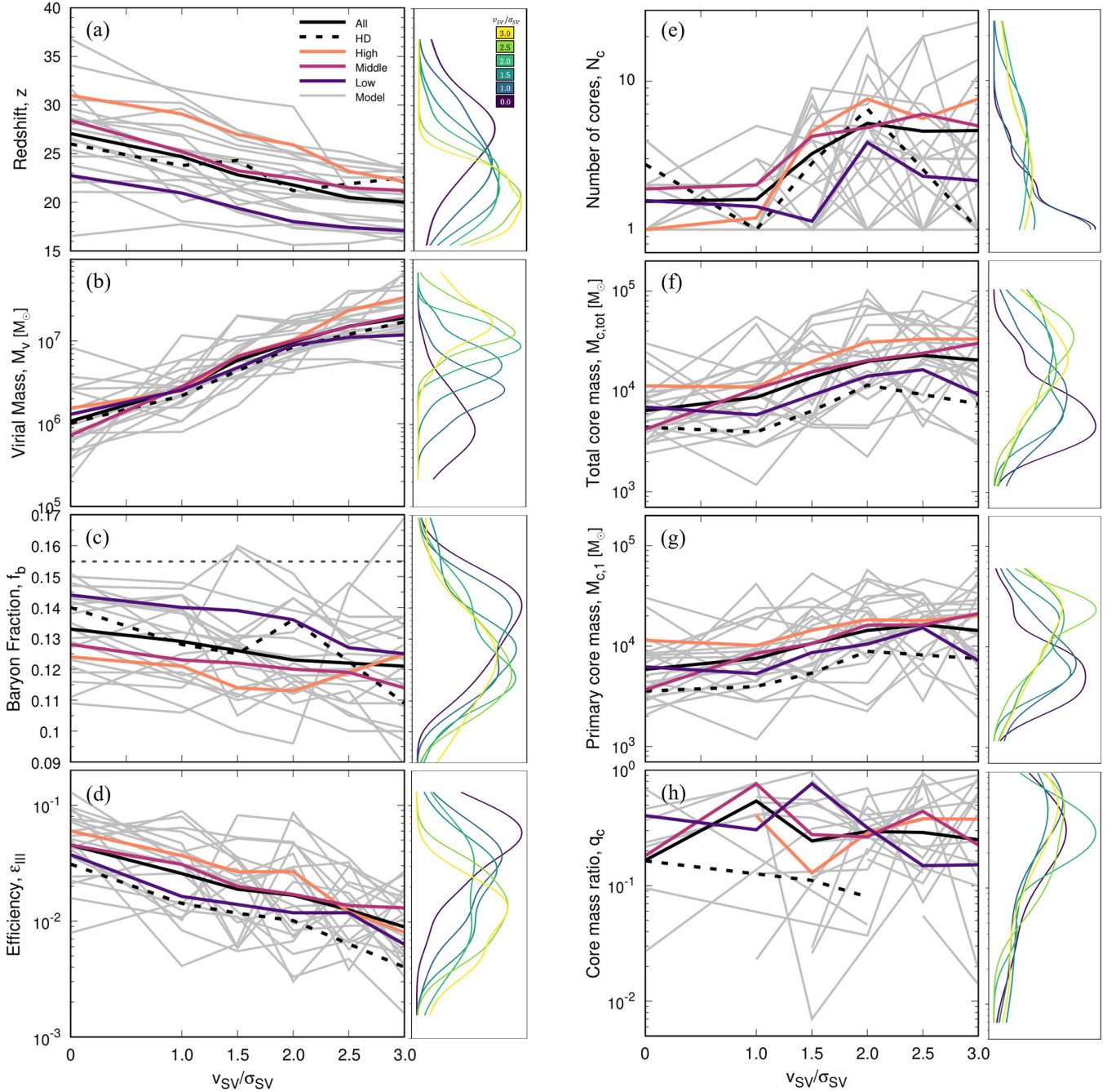


Figure 6. Initial streaming velocity dependence of the calculation results. Panels: (a) formation redshift, (b) halo mass, (c) baryon fraction (the horizontal dotted line shows the cosmic mean $\Omega_b/\Omega_m = 0.15484$), (d) mass conversion efficiency, (e) number of cores, (f) total mass of cores, (g) primary core mass, and (h) mass ratio of the primary and secondary cores. The solid and dashed lines show the results averaged over all models (*All*) and models with HD-cooling enabled (*HD*). The dashed line in the panel (h) ends up at $v_{SV}/\sigma_{SV} = 2.0$ because some parameters have no corresponding model (Table 1). The coloured lines show the averaged results for three classified groups: *High*, *Middle*, and *Low*. The grey lines show the results for each series (I01-I20). The small panel on the right shows the probability density distribution for each initial streaming velocity as in Figure 3.

formation redshift and mass, we created radial profiles for each of the three classified groups: *High*, *Middle*, and *Low*.

Figure 7(a-c) shows the gas (baryon) and DM density distributions at the end of the collapse phase ($t_{th} = 0$ yr). Higher SV typically leads to more massive halos and larger radii of the DM density slope ($R \sim 100 - 500$ pc). Gas densities surpass DM densities at some radius ($R \sim 10$ pc, $n \sim 10^2 - 10^3$ cm $^{-3}$), but the exact crossing point

depends on SV and halo class. High SV tends to flatten the DM cusp into a core-like structure, shifting the gas-DM density crossing point outward and to lower densities. This can facilitate the formation of large-scale sheets and filaments (Figure 5) since gas collapses without being tightly bound by a steep DM potential well.

Figure 7(d-f) shows the temperature distribution of the gas clouds at the onset of the accretion phase ($t_{th} = 0$ yr) and at the end of

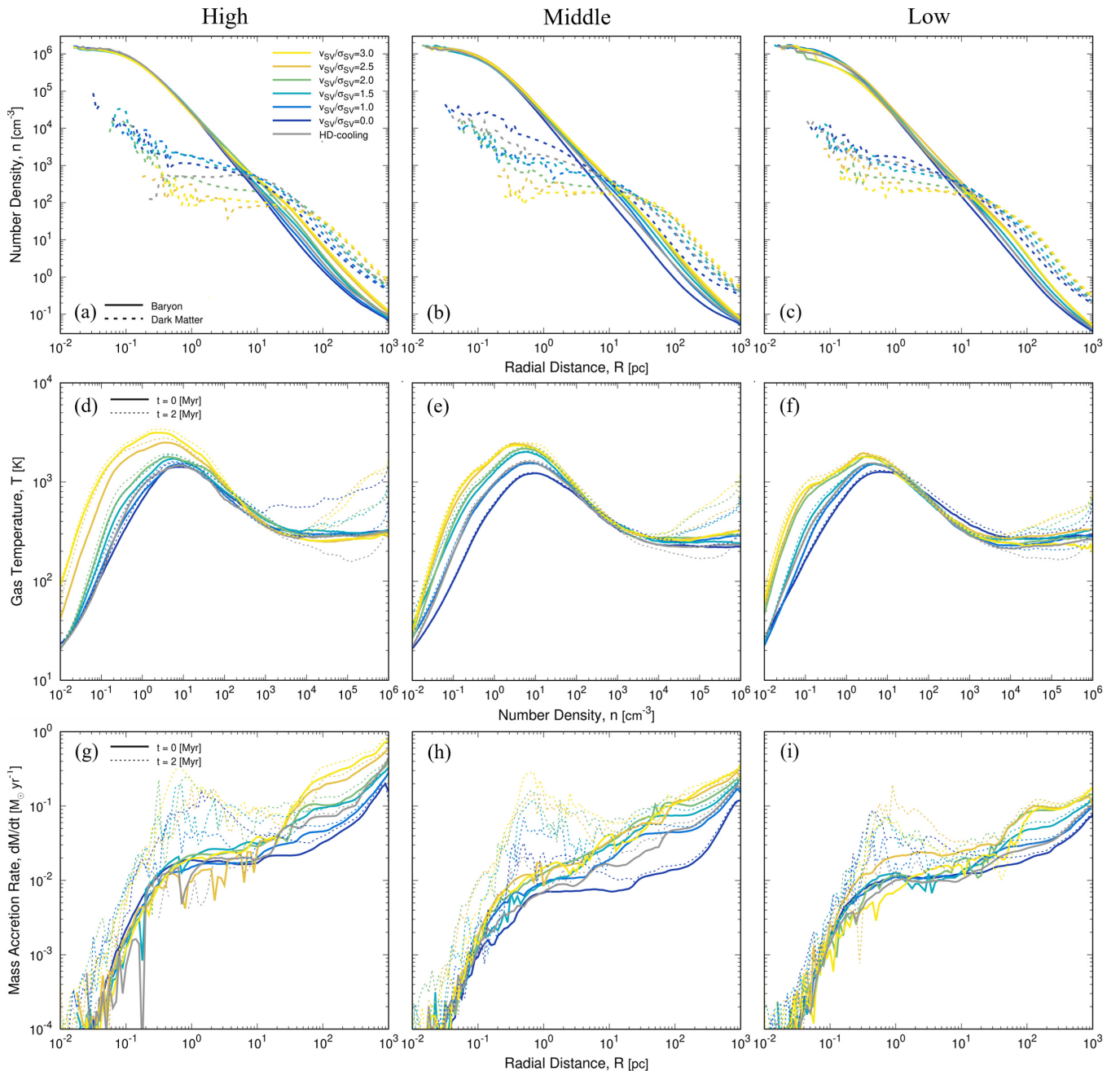


Figure 7. Profiles averaged across models belonging to three groups (*High*, *Middle*, and *Low*) for the same initial streaming velocity. Panels: (a-c) radial profile of baryon (gas; solid lines) and dark matter (dashed) density when $t_{\text{th}} = 0$ Myr, (d-f) density profile of gas temperature when $t_{\text{th}} = 0$ Myr (solid) and $t_{\text{th}} = 2$ Myr (dashed), and (g-i) radial profile of gas mass accretion rate when $t_{\text{th}} = 0$ Myr (solid) and $t_{\text{th}} = 2$ Myr (dashed). The coloured lines show averaged profiles for each initial streaming velocity (V00-30), whereas the grey lines represent the HD-cooling models (see Table A1).

the simulation ($t_{\text{th}} = 2$ Myr). Gas clouds are accumulated by the halo’s gravity and undergo adiabatic compression as n increases ($n \rightarrow 1 \text{ cm}^{-3}$). At this stage, gas temperatures increase with SV magnitude, corresponding to increases in virial mass and virial temperature. Furthermore, the *High* class is more strongly affected by SV compared to the *Middle* and *Low* classes. As gas density increases ($n > 1 \text{ cm}^{-3}$), the gas cools and contracts via H_2 -cooling. At this stage, the gas temperature does not show a clear dependence on SV.

Figure 7(g-i) shows the mass accretion rate of the gas clouds ($dM/dt = 4\pi r^2 n v_{\text{rad}}$). Higher SV generally leads to increased ac-

cretion rates at the outer scales of the gas cloud (minihalo scale, $R > 10$ pc). Conversely, at inner scales, at $t_{\text{th}} = 0$ yr, the influence of SV is minimal. However, by $t_{\text{th}} = 2$ Myr, the accretion rates around the dense core increase, with slightly higher accretion rates observed for larger SV values. When dividing the models into three classes, the overall accretion rate decreases in the order of *High*, *Middle*, and *Low*. This suggests that gas clouds forming from high-redshift, high-mass halos, those with denser density fluctuations influenced by high SV, exhibit higher accretion rates.

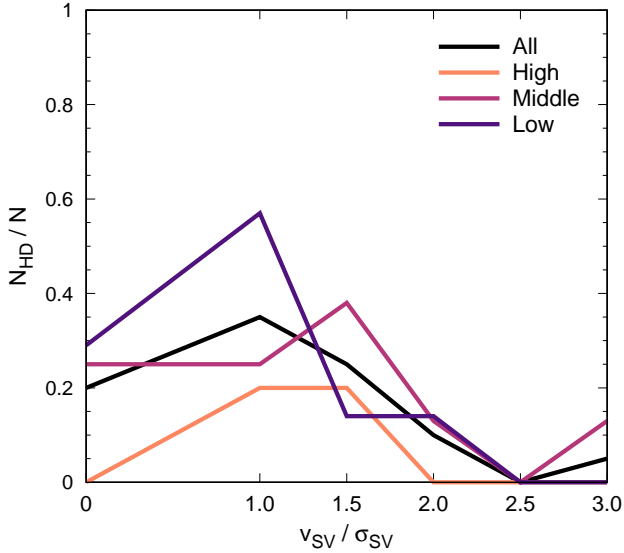


Figure 8. Initial streaming velocity dependence of the proportion of the HD-cooling models that meet the abundance ratio criterion $f_{\text{HD}}/f_{\text{H}_2} \geq 10^{-3}$ at the end of the calculation $t_{\text{th}} = 2$ Myr. The black line shows the results averaged over all models (*All*), whereas the coloured lines show the averaged results for three classified groups (*High*, *Middle*, and *Low*).

3.2.1 HD-cooling

Besides H_2 , hydrogen deuteride (HD) is also vital for first star formation (e.g., Hirano et al. 2014). We determined whether a model exhibits effective HD-cooling by setting the condition that the chemical abundance ratio satisfies $f_{\text{HD}}/f_{\text{H}_2} \geq 10^{-3}$ at the end of the calculation, $t_{\text{th}} = 2$ Myr, (column 8 in Table A1). Nineteen models exhibit effective HD-cooling, which can further reduce gas temperatures below the H_2 -cooling floor. Such conditions lower the Jeans mass, potentially influencing the number and mass of dense cores formed inside. As shown in Figure 7(d-i), the average temperature of HD-cooling models at $t_{\text{th}} = 2$ Myr is lower, and the accretion rate is reduced compared to the average of other models due to cooling via H_2 .

Table 1 and Figure 8 summarize the fraction of HD-cooling models in each SV class. We find that HD-cooling becomes ineffective for halos with $v_{\text{SV}}/\sigma_{\text{SV}} \geq 2$. In these systems, the higher virial temperature and reduced baryon fraction likely prevent the gas from reaching the lower temperatures required for significant HD formation. By contrast, halos with weaker SV retain higher gas densities at moderate temperatures, allowing HD to form and cool the gas below the temperature floor due to the H_2 -cooling. For example, HD-cooling becomes effective for about 60% of L10 models, which formed later with $v_{\text{SV}}/\sigma_{\text{SV}} = 1$. The average redshift of this group is $\bar{z} = 20.95$, a period when the star formation rate density (SFRD) of the first stars in the early universe was still rising. This synchronization suggests that the epoch of the most active first star formation coincides with the period when HD-cooling clouds account for more than half of all models. Consequently, low-mass first stars formed under the influence of HD-cooling may constitute a significant proportion during this epoch.¹ This suggests that HD-cooling might shift the core mass

function towards lower masses compared to the canonical first star formation scenario without considering SV.

3.3 Dense core

After the initial gravitational collapse of the first gas cloud within each model ($n = n_{\text{th}}$), we continued the simulation for an additional 2 Myr. During this period, the gravitational contraction of gas within the minihalo progresses. At this stage, the initially formed dense core where $n \geq n_{\text{th}}$ not only grows in mass through accretion but also, in some models, other regions of the primordial gas cloud undergo gravitational contraction, leading to the formation of additional dense cores (cloud-scale fragmentation). We analyzed the final number of dense cores (N_{c}) and their masses (M_{c}) at the end of the simulation ($t_{\text{th}} = 2$ Myr) for each model (Table A1). Assuming that each dense core forms one first star, N_{c} corresponds to the number of first stars, and M_{c} represents the upper mass limit of these stars.²

First, we introduce the models that exhibited particularly high fragmentation counts. Figure 9 summarizes eight models in which the number of dense cores reached $N_{\text{c}} \geq 10$ by the end of the simulation. Arranged in order of N_{c} from top left to right and then bottom left to right, the top panels display the 3D distribution of dense cores. Dense cores are formed along filaments with lengths of several tens of parsecs (up to 50 pc in model I11V30). Observing the temporal evolution, we confirmed that dense cores move along the filaments and approach each other. We also observed cases where multiple dense cores merged within the 2 Myr. In models I10V30 and I06V30, dense core clusters independently form in distant regions of the filament. The bottom panels show the mass distribution of dense cores, which spans a wide range from $M_{\text{c}} = 10 - 10^5 M_{\odot}$. Notably, multiple massive dense cores with $M_{\text{c}} \geq 10^4 M_{\odot}$ are formed. These massive cores acquire mass through the accretion of surrounding gas and mergers with other cores. Each is thought to host a massive first star. Additionally, we observed massive dense cores on the same filament approaching each other.

From Table 1, we can examine the dependence of the number and mass of dense cores on the magnitude of SV. The right-side sub-panels represent the distribution for each SV magnitude, illustrating SV's impact on each physical quantity. For N_{c} (Figure 6e), we find a wide diversity in the number of cores formed by 2 Myr. Some halos remain monolithic, producing only a single core, while others fragment extensively, hosting more than 10 cores along elongated filaments. Multiple fragmentation events are particularly common in halos that collapse at intermediate redshifts and have moderate SV values, conditions in which large-scale filamentary structures can grow. Comparisons of N_{c} , total core mass ($M_{\text{c,tot}}$; Figure 6f), and the primary core mass ($M_{\text{c,1}}$; Figure 6g) reveal that while SV strongly influences the number of cores, the mass of cores remains broadly similar across the *High*, *Middle*, and *Low* classes. Figure 6(h) plots q_{c} , the mass ratio of the primary and secondary cores. As SV increases, q_{c} slightly decreases, generally around $q_{\text{c}} \sim 0.3$. Large filaments sometimes host multiple cores with substantial masses, potentially serving as progenitors of star clusters or massive BH binary formation sites.

Figure 10 summarizes the core mass function (CMF) of models

nal photo-dissociation, which is not considered in this study, on HD-cooling clouds is discussed in (Nishijima et al. 2024).

² However, if disk-scale fragmentation occurs, a single dense core may host multiple first stars (e.g., Susa 2019; Sugimura et al. 2023). In such cases, M_{c} can be considered the upper limit of the total mass of multiple first stars.

¹ Lenoble et al. (2024) recently discussed the relationship between HD-cooling and slow contraction by halo spin. Furthermore, the impact of exter-

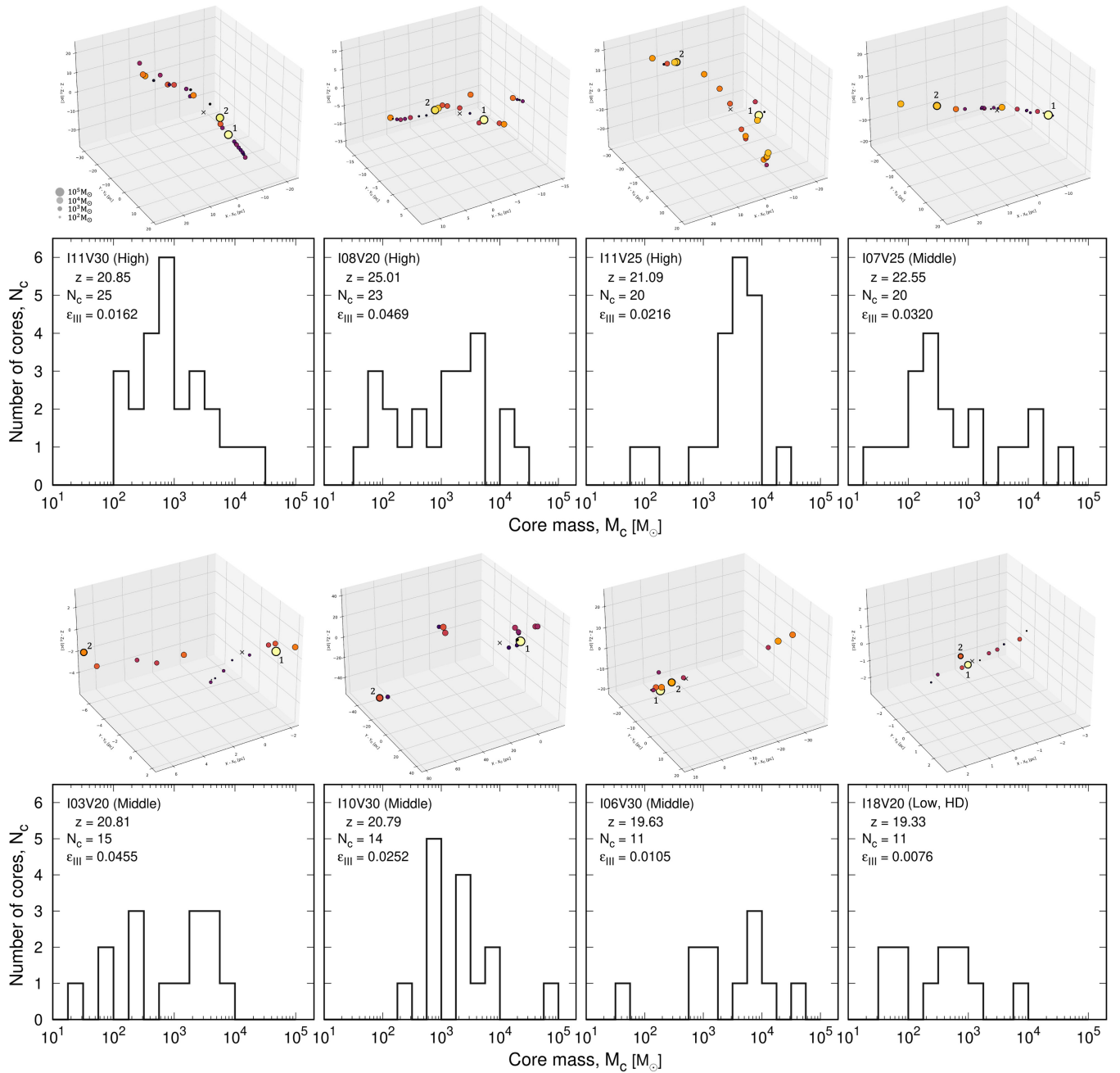


Figure 9. Core mass distribution for 8 models with large $N_c \geq 10$. We also plot the spatial distribution of the cores for each system. The larger the core mass, the larger the symbol’s radius and the redder the symbol’s colour. We have distinguished the primary core, which has the largest mass in the system, and the secondary core, which has the second largest core mass, by indexing them as “1” and “2”.

with multiple dense core formations ($N_c \geq 3$) at the end of the simulation. The overall average (black solid line) exhibits a nearly flat slope across $M_c = 5 \times (10^2 - 10^3) M_\odot$. Additionally, a sub-peak appears at $M_c = 2 \times 10^4 M_\odot$, indicating that primary cores have grown to massive masses. The formation epochs (*High*, *Middle*, and *Low*) do not significantly impact the CMF. SV’s main role is to set the fragmentation mode (single versus multiple cores) rather than imposing a fundamentally different CMF shape. In models that underwent extensive fragmentation with $N_c \geq 10$ (dashed line in Figure 9), the sub-peak at $\sim 2 \times 10^4 M_\odot$ in the CMF disappears. In HD-cooling models (*HD*; dotted line), the distribution shifts towards

the lower mass side compared to the average mass function, and massive cores with $M_c > 10^4 M_\odot$ do not form.

4 FORMATION CRITERION OF THE FIRST STAR CLUSTERS

A set of simulation results shows that SV governs a cascade of changes, from the halo formation epoch and mass to the thermodynamics and accretion dynamics of the Jeans-scale gas cloud and finally to the number and mass distribution of dense cores. While the overall fragmentation behaviour depends on multiple factors (e.g.,

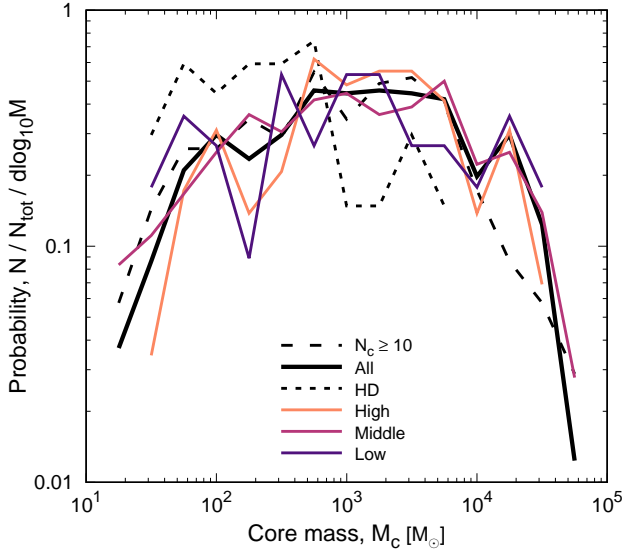


Figure 10. Mass function of dense cores when $t_{\text{th}} = 2 \text{ Myr}$ normalized by $d \log_{10} M_c = 0.25$. We have combined the functions of models with $N_c \geq 3$ for five classes: *All*, *HD*, *High*, *Middle*, and *Low*. The dashed line represents the combined function for models with large $N_c (\geq 10)$.

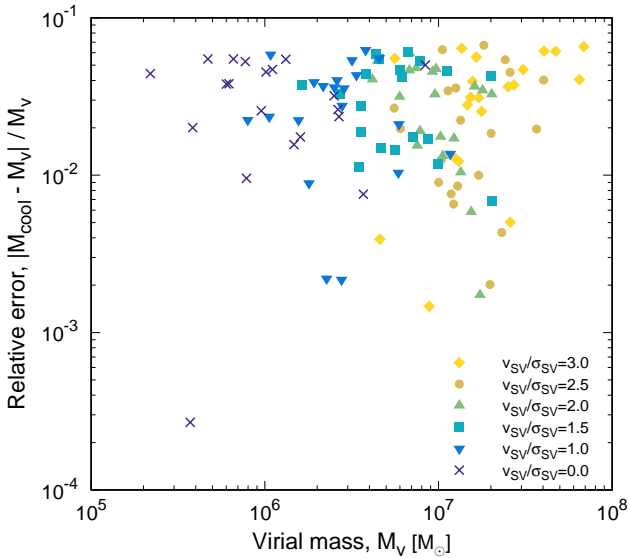


Figure 11. Relative error of the cooling threshold mass to the halo mass. We assign the value obtained from the analysis of the simulation data to the circular velocity in Equation 4.

halo density fluctuations, cooling physics, etc.), SV emerges as a key parameter controlling whether the first star-forming regions produce a solitary massive star or a cluster of proto-stellar cores.

The simulation set presents that the halo mass and number of cores vary with the initial SV value. This section formulates and qualitatively understands the dependences on the initial SV value.

4.1 Critical halo mass

Figure 3 shows how the host halo mass at the onset of cloud collapse (the so-called critical halo mass) depends on SV. This crit-

ical halo mass is a key parameter for semi-analytical modelling (e.g., [Feathers et al. 2024](#)). Using Kernel Density Estimation (KDE; coloured areas) based on our sample of halos, we confirm that the redshift dependence of the virial mass M_v varies systematically with increasing SV. This trend is notably different from any previous results in the literature, making it a novel feature in our analysis. Motivated by this, we attempt to fit our data to the same type of function used in [Hirano et al. \(2018\)](#), which examined only three models with different SV for a single halo.

We define the critical halo mass, M_{crit} , as the virial mass M_v at the onset of the gas collapse. This threshold closely matches the so-called cooling threshold mass M_{cool} , defined at the characteristic temperature $T_v = 1000 \text{ K}$:

$$M_{\text{cool}} = 1.2 \times 10^6 M_{\odot} \left(\frac{v_{\text{circ}}}{6 \text{ km s}^{-1}} \right)^3 \left(\frac{1+z}{25} \right)^{-3/2}, \quad (4)$$

where $v_{\text{circ}} = \sqrt{GM_v/R_v}$ is the circular velocity, G is the gravitational constant, and M_v and R_v are the virial mass and radius, respectively (e.g., [Barkana & Loeb 2001](#)).

Before proceeding with the fitting, we verify that the halo dynamics characterized by v_{circ} can reliably represent the cooling threshold mass. To do this, we compare M_{cool} to the measured M_{vir} for our 120 models and compute their relative differences (Figure 11). We find that, regardless of the SV value, the relative error is less than 10% for all models. Thus, if we can construct a suitable fitting function for v_{circ} , we can reliably determine M_{crit} .

[Fialkov et al. \(2012\)](#) proposed a formulation for the increase in the critical halo mass by introducing an “effective” velocity:

$$v_{\text{circ}} = \sqrt{v_{\text{circ},0}^2 + [\alpha v_{\text{SV}}(z)]^2}, \quad (5)$$

where $v_{\text{circ},0}$ and α are fitting parameters. Using our sample, we re-fit these parameters and find $v_{\text{circ},0} = 6.0 \text{ km s}^{-1}$ and $\alpha = 7.8$, which best reproduce our results.³ Figure 12 shows the resulting relations between v_{circ} , M_{crit} , and M_v . Although the overall trends are captured, panels (a) and (c) reveal significant scatter around the fitting lines. Panels (b) and (d) show that relative errors can sometimes reach a factor of 3.

A key difference compared to earlier fitting functions is that, at high SV and high z , M_{crit} decreases with increasing redshift, reflecting the structure of the KDE in Figure 3. This behaviour can also explain the presence of models that far exceed the conventional upper mass limit for H-cooling halos.

One possible interpretation is that at high redshifts, mergers of minihalos introduce additional complexity. Simple temperature thresholds like $T_v = 1000 \text{ K}$ may not fully capture the evolutionary dynamics (e.g., “violent merger delay” scenario [Inayoshi et al. 2018; Wise et al. 2019](#)). Preliminary investigations into even higher-redshift, more massive halos suggest that a higher virial temperature threshold, such as $T_v = 8000 \text{ K}$, might better explain these systems.

4.2 Formation criterion of the first star cluster

To investigate the formation criterion of the first star cluster, we focus on the mass distribution of dense cores at 2 Myr after the onset of the star-forming region, rather than directly counting the number of actual first stars. Since these cores emerge from the fragmentation of large-scale filaments and sheets, the core mass distribution provides

³ For comparison, [Hirano et al. \(2018\)](#) reported $v_{\text{circ},0} = 3.7 \text{ km s}^{-1}$ and $\alpha = 4.0$.

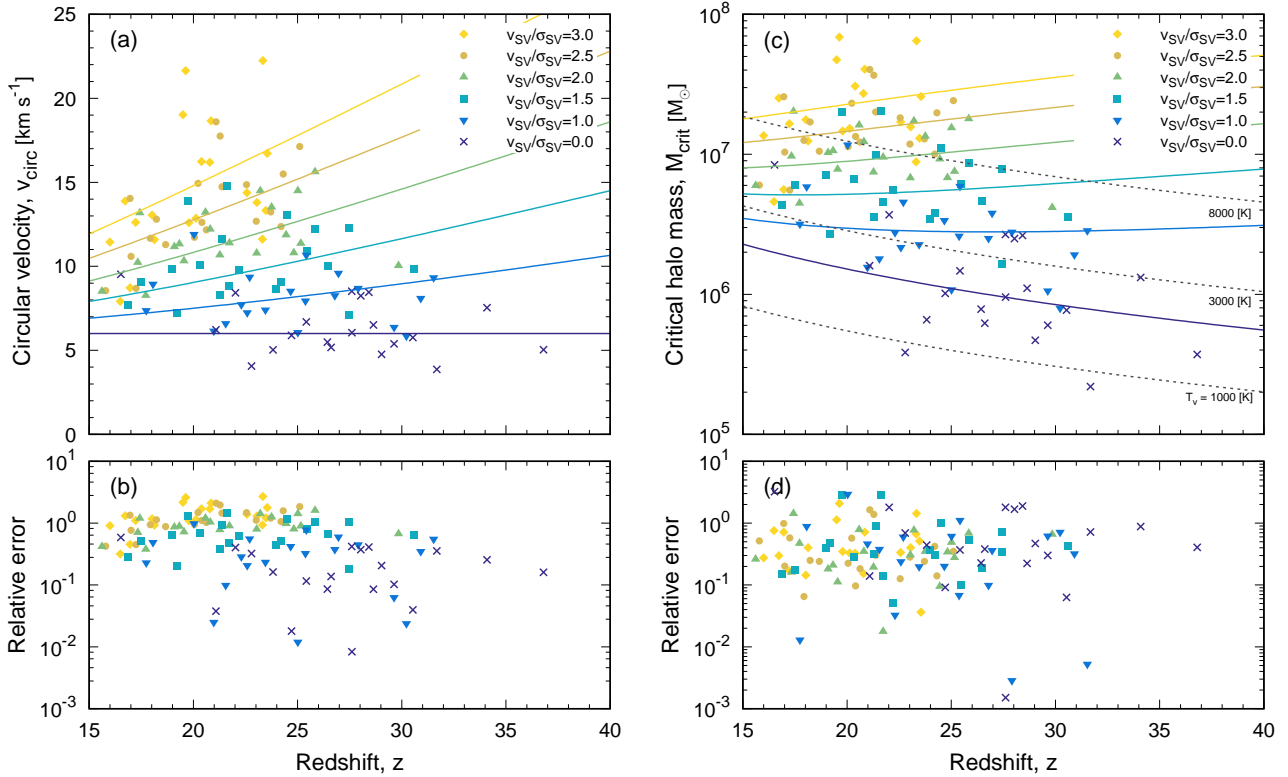


Figure 12. Fitting functions of circular velocity (Equation 5, left panels) and critical halo mass (as Equation 4, right) with $v_{\text{circ},0} = 6.0 \text{ km s}^{-1}$, $\alpha = 7.8$. The top panels compare the fitting functions and simulation results. The bottom panels show the relative error of the fitting functions to the simulation results. The dashed lines in panel (c) indicate the virial masses for three different virial temperatures, $T_v = 1000, 3000,$ and 8000 K (Equation 3).

an upper-limit criterion for identifying potential massive first star clusters.

We next examine how the number of cores (N_c) depends on the baryonic streaming velocity (SV). As shown in Figure 6(e), a clear transition occurs at around $v_{\text{SV}}/\sigma_{\text{SV}} = 1.5$: systems with lower SV values produce only a single core, while those above this threshold form multiple cores. This transition is also evident in the frequency distributions (see the inset panel), highlighting a change from single to multiple core formation regimes. At $v_{\text{SV}}/\sigma_{\text{SV}} \geq 1 - 1.5$, the thermal structure (e.g., $T_{\text{max}}/T_{\text{mix}}$ Hirano et al. 2023) and density evolution produce more extensive sheets and filaments (Figure 7). The fragmentation of these massive filaments leads to the simultaneous formation of multiple cores along their length (Figure 5 and 10). We also find indications that HD-cooling can enhance fragmentation, particularly in cases without SV.

To quantify the parameter space for multiple core formation, we plot the N_c distributions for each SV value in Figure 13(a). As discussed, at $v_{\text{SV}}/\sigma_{\text{SV}} \geq 1.5$, we observe a marked increase in N_c . Higher halo mass or redshift environments (*High* and *Middle*) also tend to produce more cores than *Low* ones.

We overlay the probability density function of v_{SV} onto our results. Around the cosmic mean SV amplitude of $v_{\text{SV}}/\sigma_{\text{SV}} \approx 0.8$, the star-forming behaviour is essentially indistinguishable from the no-SV scenario. Thus, in about 90% of cases (with $v_{\text{SV}}/\sigma_{\text{SV}} < 1.5$), the conventional 1 halo-1 cloud scenario remains valid. Only a few per cent of cases (with $v_{\text{SV}}/\sigma_{\text{SV}} \geq 1.5$) experience a 1 halo-multiple cloud regime, producing on average $N_c \sim 4$ (Table 1), and occasionally $N_c \geq 10$ (Table A1).

In high-redshift, high- M_v regimes not examined in this study, previous work (Hirano et al. 2017) has shown that the collapse may lead to a single supermassive star. In that upper-right region of the z - M_v parameter space, filaments fail to fragment into multiple cores, instead experiencing rapid collapse that supports a high accretion rate onto a single object. Consequently, the formation of first star clusters appears to be a phenomenon restricted to intermediate regions of the z - M_v parameter space, where filament collapse is not as dominant, allowing multiple cores, and thus potential first star clusters, to form.

4.3 Mass conversion efficiency

Finally, we examine the gas-to-core mass ratio, treating it as an upper limit on the gas-to-star conversion efficiency within the halo. Figure 6(d). This ratio decreases with increasing v_{SV} , (the mean values at each v_{SV} , decrease from 4.53% to 0.89%; Table 1). It also decreases as the amplitude of density fluctuations becomes larger, from *High* to *Middle* to *Low*. The efficiency tends to decline at lower redshifts for models with larger v_{SV} values. Moreover, models with effective HD-cooling show the lowest efficiency among them.

Figure 13(b). We plot the distribution of this ratio for each v_{SV} , together with the probability distribution of v_{SV} itself. At the most common values, over 80% of the systems have efficiencies of 1 – 10%. Although this fraction decreases with increasing v_{SV} , it is only marginally evident within the current plot resolution.

We interpret these results as follows. To maintain a high star formation efficiency, the entire large-scale, massive filament must undergo a nearly uniform density increase. In reality, only the regions with

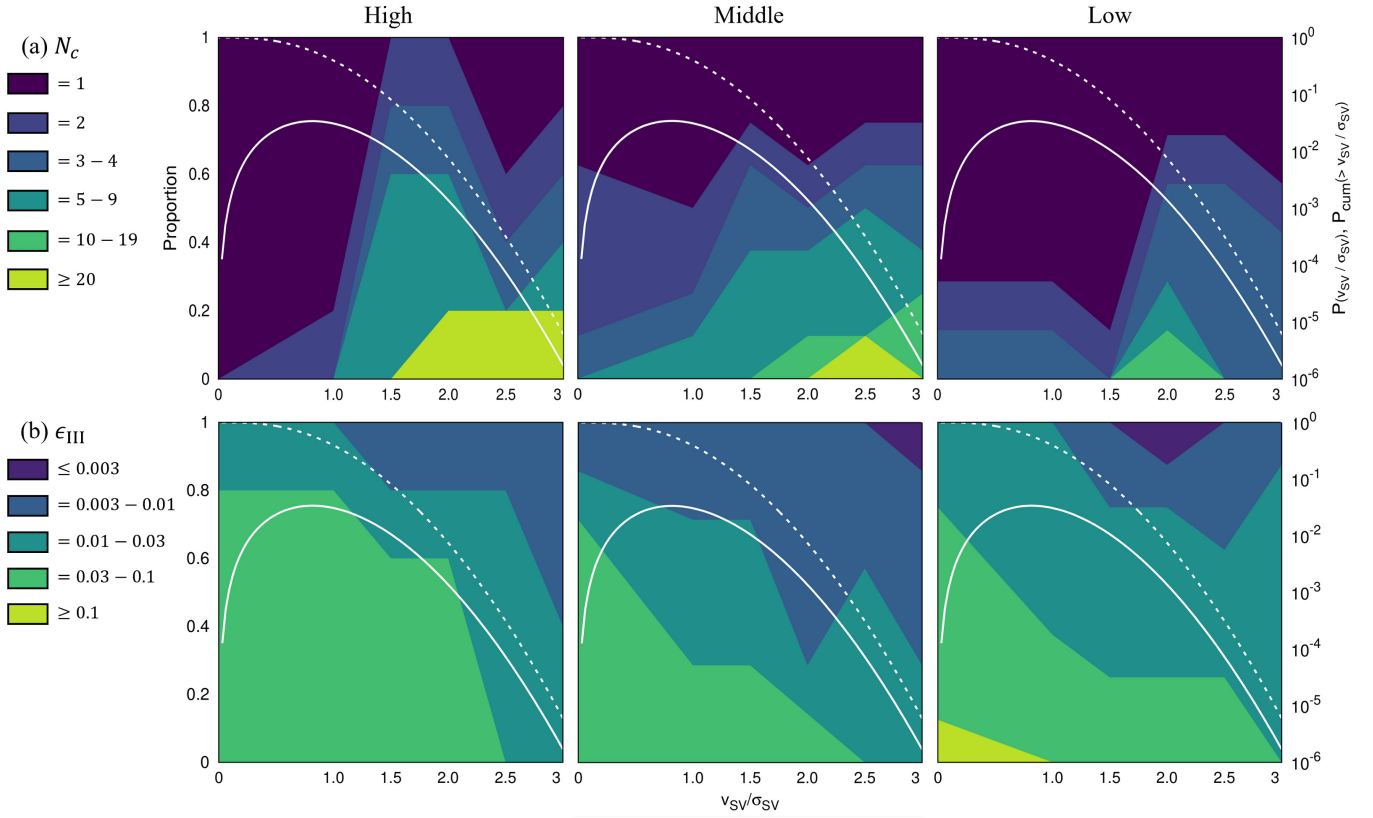


Figure 13. Dependence of the proportions of the number of cores (N_c) and mass conversion efficiency (ϵ_{III}) on the initial streaming velocity for three classes (*High*, *Middle*, and *Low*). The white lines show the probability distribution of the streaming velocity (solid; Equation 13 in [Tselikhovich et al. 2011](#)) and the cumulative one (dashed).

strong density perturbations grow non-linearly first, so after 2 Myr of evolution, only a portion of the filament has become a dense gas cloud. Therefore, in scenarios where large-scale filaments form (i.e., at high v_{SV}) the star formation efficiency decreases.

5 CONCLUSION

In summary, baryonic streaming velocities (SV) significantly affect the mass scale and fragmentation of the first star-forming halos. Our large sample of 120 cosmological simulations demonstrates that:

- **Higher SV** ($v_{\text{SV}}/\sigma_{\text{SV}} \geq 1.5$) delays the first star formation, shifts into more massive halos, and promotes filamentary collapse that produces multiple dense cores within a single halo.
- **Lower SV** ($v_{\text{SV}}/\sigma_{\text{SV}} \leq 1.0$) also delays the first star formation but results in a negligible impact on the cloud evolution, typically forming only one or two cores.
- **HD-cooling** is more likely to be effective under the influence of moderate SV, especially in models that form in low- z , in more than half of them. This is the parameter space in which low-mass first stars form.

These results indicate the importance of including SV in theoretical models of the cosmic dawn.⁴ In particular, the formation of multiple dense cores in a single halo could yield the first star clusters,

⁴ For instance, the most probable streaming velocity amplitude across the universe is around $v_{\text{SV}}/\sigma_{\text{SV}} \sim 0.8$ ([Tselikhovich et al. 2011](#)), whereas an

with implications for black hole seed formation and early chemical enrichment. Future work that incorporates radiative feedback, magnetic fields, and disk-scale fragmentation will be crucial for building a comprehensive model of the first star formation.

ACKNOWLEDGEMENTS

We thank Hyunbae Park for discussing the BTD approximation for the cosmological initial condition setting. Numerical computations were carried on Cray XC50 at CfCA in the National Astronomical Observatory of Japan and Yukawa-21 at YITP in Kyoto University. Numerical analyses were, in part, carried out on the analysis servers at CfCA in the National Astronomical Observatory of Japan. This work was supported by JSPS KAKENHI Grant Numbers JP21K13960 and JP21H01123 (S.H.).

DATA AVAILABILITY

The data presented in Tables 1 and A1 are publicly available at our GitHub repository: <https://github.com/shingohirano-astro/FSC2>. Additional data from this study are available from the corresponding author upon reasonable request.

analysis specific to the Milky Way region reports a value of about $v_{\text{SV}}/\sigma_{\text{SV}} \sim 1.75$ ([Uysal & Hartwig 2023](#)).

REFERENCES

- Aoki W., Tominaga N., Beers T. C., Honda S., Lee Y. S., 2014, *Science*, **345**, 912
- Aoki W., Matsuno T., Honda S., Ishigaki M. N., Li H., Suda T., Kumar Y. B., 2018, *PASJ*, **70**, 94
- Barkana R., Loeb A., 2001, *Phys. Rep.*, **349**, 125
- Bessell M. S., et al., 2015, *ApJ*, **806**, L16
- Caffau E., et al., 2011, *Nature*, **477**, 67
- Chiou Y. S., Naoz S., Marinacci F., Vogelsberger M., 2018, *MNRAS*, **481**, 3108
- Chiou Y. S., Naoz S., Burkhardt B., Marinacci F., Vogelsberger M., 2019, *ApJ*, **878**, L23
- Chiti A., et al., 2024, *Nature Astronomy*, **8**, 637
- Feathers C. R., Kulkarni M., Visbal E., Hazlett R., 2024, *ApJ*, **962**, 62
- Fialkov A., 2014, *International Journal of Modern Physics D*, **23**, 1430017
- Fialkov A., Barkana R., Tselikhovich D., Hirata C. M., 2012, *MNRAS*, **424**, 1335
- Greif T. H., White S. D. M., Klessen R. S., Springel V., 2011, *ApJ*, **736**, 147
- Hahn O., Abel T., 2011, *MNRAS*, **415**, 2101
- Harikane Y., et al., 2024, *arXiv e-prints*, p. arXiv:2406.18352
- Hirano S., Bromm V., 2017, *MNRAS*, **470**, 898
- Hirano S., Hosokawa T., Yoshida N., Umeda H., Omukai K., Chiaki G., Yorke H. W., 2014, *ApJ*, **781**, 60
- Hirano S., Hosokawa T., Yoshida N., Omukai K., Yorke H. W., 2015, *MNRAS*, **448**, 568
- Hirano S., Hosokawa T., Yoshida N., Kuiper R., 2017, *Science*, **357**, 1375
- Hirano S., Yoshida N., Sakurai Y., Fujii M. S., 2018, *ApJ*, **855**, 17
- Hirano S., Shen Y., Nishijima S., Sakai Y., Umeda H., 2023, *MNRAS*, **525**, 5737
- Inayoshi K., Li M., Haiman Z., 2018, *MNRAS*, **479**, 4017
- Keller S. C., et al., 2014, *Nature*, **506**, 463
- Kitsionas S., Whitworth A. P., 2002, *MNRAS*, **330**, 129
- Klessen R. S., Glover S. C. O., 2023, *ARA&A*, **61**, 65
- Kulkarni M., Visbal E., Bryan G. L., 2021, *ApJ*, **917**, 40
- Lenoble R., Commerçon B., Rosdahl J., 2024, *arXiv e-prints*, p. arXiv:2401.16821
- Mardini M. K., Frebel A., Chiti A., 2024, *MNRAS*, **529**, L60
- Naoz S., Narayan R., 2014, *ApJ*, **791**, L8
- Nishijima S., Hirano S., Umeda H., 2024, *ApJ*, **965**, 141
- Park H., Ahn K., Yoshida N., Hirano S., 2020, *ApJ*, **900**, 30
- Park H., Shapiro P. R., Ahn K., Yoshida N., Hirano S., 2021, *ApJ*, **908**, 96
- Placco V. M., et al., 2016, *ApJ*, **833**, 21
- Placco V. M., et al., 2021, *ApJ*, **912**, L32
- Planck Collaboration et al., 2020, *A&A*, **641**, A6
- Robertson B., et al., 2024, *ApJ*, **970**, 31
- Rossi M., Salvadori S., Skúladóttir Á., Vanni I., Koutsouridou I., 2024, *arXiv e-prints*, p. arXiv:2406.12960
- Schaerer D., 2002, *A&A*, **382**, 28
- Schauer A. T. P., Glover S. C. O., Klessen R. S., Clark P., 2021, *MNRAS*, **507**, 1775
- Schneider R., Omukai K., Limongi M., Ferrara A., Salvaterra R., Chieffi A., Bianchi S., 2012, *MNRAS*, **423**, L60
- Skúladóttir Á., et al., 2021, *ApJ*, **915**, L30
- Springel V., 2005, *MNRAS*, **364**, 1105
- Stacy A., Bromm V., Loeb A., 2011, *ApJ*, **730**, L1
- Sugimura K., Matsumoto T., Hosokawa T., Hirano S., Omukai K., 2023, *ApJ*, **959**, 17
- Susa H., 2019, *ApJ*, **877**, 99
- Tselikhovich D., Hirata C., 2010, *Phys. Rev. D*, **82**, 083520
- Tselikhovich D., Barkana R., Hirata C. M., 2011, *MNRAS*, **418**, 906
- Uysal B., Hartwig T., 2023, *MNRAS*, **520**, 3229
- Wise J. H., Regan J. A., O’Shea B. W., Norman M. L., Downes T. P., Xu H., 2019, *Nature*, **566**, 85
- Xing Q.-F., et al., 2023, *Nature*, **618**, 712
- Yoshida N., Oh S. P., Kitayama T., Hernquist L., 2007, *ApJ*, **663**, 687
- Yoshida N., Omukai K., Hernquist L., 2008, *Science*, **321**, 669

APPENDIX A: RESULTS OF 120 MODELS

This paper has been typeset from a $\text{\TeX}/\text{\LaTeX}$ file prepared by the author.

Table A1. Parameters and results of 120 models

Model	v_{SV}/σ_{SV}	z	R_v (pc)	M_v (M_\odot)	f_b	Class	HD	N_c	$M_{c,tot}$ (M_\odot)	ϵ_{III}	$M_{c,1}$ (M_\odot)	$M_{c,2}$ (M_\odot)	q_c
I01V00	0.0	36.80	63.1	3.723×10^5	0.109	<i>High</i>		1	3882	0.0958	3882	-	-
I01V10	1.0	30.91	125.9	1.920×10^6	0.106		Y	1	9567	0.0469	9567	-	-
I01V15	1.5	27.45	223.9	7.856×10^6	0.114		Y	2	5253	0.0059	5122	131	0.026
I01V20	2.0	25.84	316.2	1.794×10^7	0.118			5	45957	0.0218	29131	6038	0.207
I01V25	2.5	25.10	354.8	2.419×10^7	0.109			1	46198	0.0175	46198	-	-
I01V30	3.0	23.33	562.3	6.468×10^7	0.121			7	42438	0.0054	33401	3292	0.099
I02V00	0.0	34.09	100.0	1.319×10^6	0.121	<i>High</i>		1	8635	0.0542	8635	-	-
I02V10	1.0	31.53	141.3	2.855×10^6	0.108			1	19714	0.0638	19714	-	-
I02V15	1.5	30.60	158.5	3.576×10^6	0.100			7	18935	0.0528	14945	1765	0.118
I02V20	2.0	29.84	177.8	4.163×10^6	0.096			2	19186	0.0481	16122	3065	0.190
I02V25	2.5	21.28	501.2	3.670×10^7	0.146			4	60304	0.0113	22010	20668	0.939
I02V30	3.0	19.50	562.3	4.732×10^7	0.169			2	33990	0.0043	23552	10439	0.443
I03V00	0.0	31.68	63.1	2.195×10^5	0.111	<i>Middle</i>		1	3158	0.1295	3158	-	-
I03V10	1.0	20.03	354.8	1.169×10^7	0.125			3	47059	0.0321	41683	5276	0.127
I03V15	1.5	21.37	316.2	9.943×10^6	0.127	<i>E1</i>	Y	1	7381	0.0058	7381	-	-
I03V20	2.0	20.81	354.8	1.229×10^7	0.124			15	69239	0.0455	44308	6124	0.138
I03V25	2.5	20.41	354.8	1.341×10^7	0.125			6	49196	0.0293	26382	21452	0.813
I03V30	3.0	20.13	398.1	1.531×10^7	0.124			3	26778	0.0141	25882	493	0.019
I04V00	0.0	30.53	100.0	7.717×10^5	0.116	<i>Middle</i>		2	4560	0.0511	4441	119	0.027
I04V10	1.0	30.22	100.0	7.972×10^5	0.114			1	2781	0.0306	2781	-	-
I04V15	1.5	27.45	141.3	1.647×10^6	0.128		Y	8	5912	0.0280	3203	997	0.311
I04V20	2.0	24.82	251.2	6.800×10^6	0.109			1	2243	0.0030	2243	-	-
I04V25	2.5	23.02	316.2	1.183×10^7	0.113			2	13813	0.0103	9544	4269	0.447
I04V30	3.0	23.31	281.8	8.841×10^6	0.089	<i>E1</i>		1	21215	0.0270	21215	-	-
I05V00	0.0	29.63	89.1	6.011×10^5	0.123	<i>Middle</i>		1	3081	0.0416	3081	-	-
I05V10	1.0	26.96	177.8	3.807×10^6	0.116		Y	1	4500	0.0102	4500	-	-
I05V15	1.5	25.45	223.9	6.182×10^6	0.112			9	56412	0.0818	23528	16669	0.708
I05V20	2.0	24.45	281.8	9.226×10^6	0.106			8	71629	0.0734	46693	18986	0.407
I05V25	2.5	23.71	316.2	1.288×10^7	0.100			7	45237	0.0351	33732	5872	0.174
I05V30	3.0	23.05	354.8	1.571×10^7	0.100			3	17258	0.0110	6948	6002	0.864
I06V00	0.0	29.03	89.1	4.698×10^5	0.119	<i>Middle</i>		1	2404	0.0429	2404	-	-
I06V10	1.0	25.01	125.9	1.079×10^6	0.119		Y	1	3981	0.0309	3981	-	-
I06V15	1.5	23.97	199.5	3.465×10^6	0.111		Y	2	8391	0.0219	6766	1624	0.240
I06V20	2.0	21.73	316.2	9.533×10^6	0.122			3	15988	0.0137	11579	3003	0.259
I06V25	2.5	20.62	354.8	1.222×10^7	0.116			3	9198	0.0065	7232	1568	0.217
I06V30	3.0	19.63	631.0	6.869×10^7	0.117			11	84097	0.0105	44502	10855	0.244
I07V00	0.0	28.64	112.2	1.106×10^6	0.129	<i>Middle</i>	Y	2	3000	0.0210	2050	949	0.463
I07V10	1.0	26.79	158.5	2.514×10^6	0.117			2	11161	0.0380	6444	4717	0.732
I07V15	1.5	21.61	398.1	2.030×10^7	0.110			6	45839	0.0206	18220	17657	0.969
I07V20	2.0	23.21	354.8	1.731×10^7	0.114	<i>E1</i>		7	57912	0.0294	31496	9606	0.305
I07V25	2.5	22.55	354.8	1.822×10^7	0.109			20	63743	0.0320	32817	12111	0.369
I07V30	3.0	22.57	354.8	1.705×10^7	0.109	<i>E1</i>	Y	1	7494	0.0040	7494	-	-

Notes. Same as Table 1 but for each model. Column 1: model name. Models I01, I04, I10, I11, I13, I14, and I19 correspond to Halos A, B, C, D, E, F, and G in Paper I. Column 4: radius (R_v) at the virial scale. We determine the virial radii from distance grids, divided into 20 grids with one order of magnitude of distance on a logarithmic scale, so the same values appear in the table. Column 7: Class names as three classes for each model series (*High*, *Middle*, and *Low* as described in Section 3) in columns of no-SV models whereas three exceptional SV dependence on z - M_v diagram (*E1*, *E2*, and *E3* as described in Section 3.1.1) in columns of models with SV. Column 8: whether HD-cooling is enabled (abundance ratio criterion, $f_{HD}/f_{H_2} \geq 10^{-3}$) at the end of the calculation. Column 13: mass of the secondary core ($M_{c,2}$). Column 14: mass ratio of the primary and secondary core ($q_c = M_{c,2}/M_{c,1}$). There is no data in columns 13 and 14 for models with $N_c = 1$ because there is no secondary core.

Table A1 – continued

Model	v_{SV}/σ_{SV}	z	R_V (pc)	M_V (M_\odot)	f_b	Class	HD	N_c	$M_{c,tot}$ (M_\odot)	ϵ_{III}	$M_{c,1}$ (M_\odot)	$M_{c,2}$ (M_\odot)	q_c
I08V00	0.0	28.42	158.5	2.637×10^6	0.130	<i>High</i>		1	30352	0.0887	30352	-	-
I08V10	1.0	27.91	158.5	2.786×10^6	0.132			1	14592	0.0397	14592	-	-
I08V15	1.5	25.85	251.2	8.700×10^6	0.128			5	57294	0.0515	52925	1516	0.029
I08V20	2.0	25.01	316.2	1.543×10^7	0.115			23	83535	0.0469	26394	15624	0.592
I08V25	2.5	24.31	354.8	1.980×10^7	0.106			1	32946	0.0157	32946	-	-
I08V30	3.0	23.55	398.1	2.587×10^7	0.097			3	12589	0.0050	6296	5708	0.907
I09V00	0.0	28.03	158.5	2.503×10^6	0.133	<i>High</i>		1	24920	0.0750	24920	-	-
I09V10	1.0	29.63	112.2	1.061×10^6	0.118	<i>EI</i>		1	5025	0.0402	5025	-	-
I09V15	1.5	26.45	199.5	4.638×10^6	0.121			5	13707	0.0245	6391	5219	0.817
I09V20	2.0	25.16	251.2	7.538×10^6	0.118			5	34013	0.0381	21769	5673	0.261
I09V25	2.5	24.21	281.8	1.002×10^7	0.118			2	4491	0.0038	2854	1637	0.574
I09V30	3.0	23.48	316.2	1.304×10^7	0.128			1	31843	0.0191	31843	-	-
I10V00	0.0	27.61	112.2	9.544×10^5	0.143	<i>Middle</i>	Y	4	3309	0.0242	2824	269	0.095
I10V10	1.0	25.38	177.8	2.608×10^6	0.138			1	9258	0.0258	9258	-	-
I10V15	1.5	24.20	199.5	3.801×10^6	0.130			1	4787	0.0097	4787	-	-
I10V20	2.0	23.04	251.2	6.784×10^6	0.132		Y	2	12005	0.0134	11571	434	0.037
I10V25	2.5	21.37	398.1	2.009×10^7	0.148			9	42078	0.0141	16271	13344	0.820
I10V30	3.0	20.79	446.7	2.721×10^7	0.134			14	92182	0.0252	59830	6930	0.116
I11V00	0.0	27.60	158.5	2.675×10^6	0.127	<i>High</i>		1	7619	0.0223	7619	-	-
I11V10	1.0	25.42	223.9	5.918×10^6	0.140			2	11876	0.0143	7787	4089	0.525
I11V15	1.5	24.51	281.8	1.113×10^7	0.105			4	40245	0.0346	23696	12177	0.514
I11V20	2.0	23.75	316.2	1.343×10^7	0.116			3	11358	0.0073	7660	2459	0.321
I11V25	2.5	21.09	501.2	4.029×10^7	0.115			20	99898	0.0216	19532	9357	0.479
I11V30	3.0	20.85	501.2	4.055×10^7	0.108			25	71040	0.0162	21052	16954	0.805
I12V00	0.0	26.61	100.0	6.222×10^5	0.142	<i>Low</i>	Y	4	4474	0.0506	3249	769	0.237
I12V10	1.0	22.58	177.8	2.168×10^6	0.132		Y	1	1172	0.0041	1172	-	-
I12V15	1.5	20.31	281.8	6.683×10^6	0.129			1	5466	0.0064	5466	-	-
I12V20	2.0	19.09	354.8	1.027×10^7	0.117			5	102428	0.0856	57251	40004	0.699
I12V25	2.5	18.67	354.8	1.052×10^7	0.105			3	22486	0.0203	20588	1491	0.072
I12V30	3.0	18.13	398.1	1.242×10^7	0.101			4	15564	0.0125	8525	3612	0.424
I13V00	0.0	26.43	112.2	7.845×10^5	0.141	<i>Low</i>		1	8464	0.0765	8464	-	-
I13V10	1.0	23.46	177.8	2.268×10^6	0.144			3	19317	0.0590	10009	5865	0.586
I13V15	1.5	21.70	251.2	4.545×10^6	0.118			2	18468	0.0345	11888	6579	0.553
I13V20	2.0	19.55	316.2	7.821×10^6	0.112			1	8363	0.0095	8363	-	-
I13V25	2.5	17.93	398.1	1.259×10^7	0.119			2	18841	0.0125	16733	2151	0.129
I13V30	3.0	17.23	446.7	1.652×10^7	0.114			1	13916	0.0074	13916	-	-
I14V00	0.0	25.42	141.3	1.471×10^6	0.148	<i>Middle</i>		2	9274	0.0427	6777	2497	0.368
I14V10	1.0	22.70	223.9	4.561×10^6	0.138			5	55739	0.0886	23849	18663	0.783
I14V15	1.5	22.21	251.2	5.590×10^6	0.127			4	25121	0.0354	24568	175	0.007
I14V20	2.0	21.27	281.8	7.451×10^6	0.120			1	22094	0.0248	22094	-	-
I14V25	2.5	20.05	354.8	1.134×10^7	0.120			1	7717	0.0057	7717	-	-
I14V30	3.0	19.79	398.1	1.468×10^7	0.124			2	21315	0.0117	13043	8271	0.634

Table A1 – continued

Model	v_{sv}/σ_{sv}	z	R_v (pc)	M_v (M_\odot)	f_b	Class	HD	N_c	$M_{c,tot}$ (M_\odot)	ϵ_{III}	$M_{c,1}$ (M_\odot)	$M_{c,2}$ (M_\odot)	q_c
I15V00	0.0	24.71	125.9	1.016×10^6	0.135	<i>Middle</i>		2	9822	0.0717	8069	1753	0.217
I15V10	1.0	24.67	199.5	3.372×10^6	0.121			2	12668	0.0311	8947	3721	0.416
I15V15	1.5	19.74	446.7	2.000×10^7	0.131			3	31820	0.0121	19821	7676	0.387
I15V20	2.0	20.58	398.1	1.615×10^7	0.130	<i>E1</i>		1	10809	0.0052	10809	-	-
I15V25	2.5	20.22	446.7	2.315×10^7	0.123			1	19353	0.0068	19353	-	-
I15V30	3.0	20.39	501.2	3.070×10^7	0.115	<i>E2</i>		5	58686	0.0166	40081	6353	0.158
I16V00	0.0	23.82	112.2	6.588×10^5	0.143	<i>Low</i>		1	5635	0.0599	5635	-	-
I16V10	1.0	21.55	177.8	1.797×10^6	0.139			2	19840	0.0795	19392	448	0.023
I16V15	1.5	18.98	316.2	7.158×10^6	0.129			1	29981	0.0324	29981	-	-
I16V20	2.0	17.43	501.2	2.024×10^7	0.143			4	24095	0.0083	15335	7307	0.477
I16V25	2.5	16.96	562.3	2.577×10^7	0.131			3	30955	0.0091	25432	5394	0.212
I16V30	3.0	16.73	562.3	2.520×10^7	0.123	<i>E3</i>		1	28997	0.0093	28997	-	-
I17V00	0.0	22.79	100.0	3.841×10^5	0.138	<i>Low</i>		1	5141	0.0972	5141	-	-
I17V10	1.0	18.06	316.2	5.876×10^6	0.144			1	7044	0.0083	7044	-	-
I17V15	1.5	17.50	316.2	6.021×10^6	0.132			1	4376	0.0055	4376	-	-
I17V20	2.0	17.72	281.8	4.470×10^6	0.143	<i>E1</i>		1	4303	0.0067	4303	-	-
I17V25	2.5	17.25	316.2	5.552×10^6	0.130			3	21318	0.0296	20138	1108	0.055
I17V30	3.0	16.96	316.2	5.597×10^6	0.137			3	13186	0.0173	12930	177	0.014
I18V00	0.0	22.02	223.9	3.695×10^6	0.150	<i>Low</i>		1	4390	0.0079	4390	-	-
I18V10	1.0	22.30	199.5	2.768×10^6	0.148	<i>E1</i>	Y	1	6007	0.0146	6007	-	-
I18V15	1.5	21.27	223.9	3.585×10^6	0.143		Y	1	5512	0.0107	5512	-	-
I18V20	2.0	19.33	354.8	1.058×10^7	0.139		Y	11	11138	0.0076	6821	1151	0.169
I18V25	2.5	18.23	446.7	1.702×10^7	0.135			3	32918	0.0143	29685	3111	0.105
I18V30	3.0	18.02	446.7	1.768×10^7	0.130			3	7632	0.0033	3468	2118	0.611
I19V00	0.0	21.08	177.8	1.602×10^6	0.147	<i>Low</i>	Y	1	8488	0.0361	8488	-	-
I19V10	1.0	20.98	177.8	1.563×10^6	0.146	<i>E3</i>	Y	1	2814	0.0124	2814	-	-
I19V15	1.5	19.19	223.9	2.700×10^6	0.159			1	4675	0.0109	4675	-	-
I19V20	2.0	17.33	398.1	9.673×10^6	0.146			3	4608	0.0033	2599	1066	0.410
I19V25	2.5	17.01	398.1	1.038×10^7	0.137			1	6739	0.0047	6739	-	-
I19V30	3.0	16.00	446.7	1.360×10^7	0.137			2	2936	0.0016	1914	1022	0.534
I20V00	0.0	16.52	398.1	8.400×10^6	0.151	<i>Low</i>		2	20101	0.0158	11922	8179	0.686
I20V10	1.0	17.74	251.2	3.178×10^6	0.128	<i>E1</i>	Y	1	4394	0.0108	4394	-	-
I20V15	1.5	16.86	316.2	4.375×10^6	0.160			1	16003	0.0228	16003	-	-
I20V20	2.0	15.61	354.8	5.969×10^6	0.151			2	25799	0.0286	24654	1146	0.046
I20V25	2.5	15.79	354.8	6.027×10^6	0.128	<i>E2</i>		1	5324	0.0069	5324	-	-
I20V30	3.0	16.49	316.2	4.599×10^6	0.134	<i>E1</i>		1	3205	0.0052	3205	-	-